HHS Public Access

Author manuscript

Nat Cell Biol. Author manuscript; available in PMC 2020 August 06.

Published in final edited form as:

Nat Cell Biol. 2020 February ; 22(2): 225–234. doi:10.1038/s41556-020-0461-8.

Energy stress-mediated AMPK activation inhibits ferroptosis

Hyemin Lee[1,11], **Fereshteh Zandkarimi**[2,11], **Yilei Zhang**[1], **Jitendra Kumar Meena**[3], **Jongchan Kim**[1,4], **Li Zhuang**[1], **Siddhartha Tyagi**[3], **Li Ma**[1,5], **Thomas F. Westbrook**[3,7,10], **Gregory R Steinberg**[6], **Daisuke Nakada**[7], **Brent R. Stockwell**[2,8,*], **Boyi Gan**[1,5,9,*]

[1]Department of Experimental Radiation Oncology, the University of Texas MD Anderson Cancer Center, Houston, Texas 77030, USA. [2]Department of Biological Sciences, Columbia University, New York, NY 10027, USA. [3]Verna & Marrs McLean Department of Biochemistry and Molecular Biology, Baylor College of Medicine, Houston, Texas 77030, USA [4]Current address: School of Natural Sciences, Department of Life Sciences, Sogang University, Seoul, Republic of Korea [5]The University of Texas MD Anderson Cancer Center UTHealth Graduate School of Biomedical Sciences, Houston, Texas 77030, USA. [6]Centre for Metabolism, Obesity and Diabetes Research, Department of Medicine and Biochemistry and Biomedical Sciences, McMaster University, Hamilton, ON L8S 4L8, Canada. [7]Department of Molecular and Human Genetics, Baylor College of Medicine, Houston, TX 77030, USA. [8]Department of Chemistry, Columbia University, New York, NY, USA. [9]Department of Molecular and Cellular Oncology, the University of Texas MD Anderson Cancer Center, Houston, Texas 77030, USA. [10]Therapeutic Innovation Center (THINC), Baylor College of Medicine, Houston, TX 77030, USA [11]These authors contributed equally: Hyemin Lee, Fereshteh Zandkarimi.

Abstract

Energy stress depletes ATP and induces cell death. Here, we identify an unexpected inhibitory role of energy stress on ferroptosis, a form of regulated cell death induced by iron-dependent lipid peroxidation. We found that ferroptotic cell death and lipid peroxidation can be inhibited by treatments that induce or mimic energy stress. Inactivation of AMP-activated protein kinase

---

*Correspondence Authors: Boyi Gan. bgan@mdanderson.org; Phone: 713-792-8653; Fax: 713-794-5369. Brent Stockwell. bstockwell@columbia.edu; Phone: 212-854-2948.

Author contributions

H.L. performed most of the experiments with assistance from Y.Z., J.K.M., J.K. and L.Z.. F.Z. conducted lipidomic analysis under the direction of B.R.S. G.R.S. provided ACC DKI MEFs. N.D. provided *AMPKα1/α2*$^{L/L}$ MEFs and mouse model. S.T. and T.F.W. provided the inducible Cas9-vector. L.M. helped with discussion and interpretation of results. B.G. and B.R.S. designed experiments and supervised the study. B.G. wrote most of the manuscript with assistance from H.L., F.Z., and B.R.S. All authors commented on the manuscript.

Competing Interests

B.R.S. holds equity in and serves as a consultant to Inzen Therapeutics, and is an inventor on patents and patent applications related to ferroptosis. The other authors declare no competing financial interests.

Reporting summary

Further information on experimental design is available in the Nature Research Reporting Summary linked to this article

Data availability

The mass spectrometry raw data files and metadata have been deposited to the EMBL-EBI MetaboLights database with the identifier MTBLS1399 (https://www.ebi.ac.uk/metabolights/MTBLS1399). All data supporting the findings of this study are available from the corresponding author on reasonable request.

(AMPK), a sensor of cellular energy status, largely abolishes the protective effects of energy stress on ferroptosis *in vitro* and on ferroptosis-associated renal ischemia/reperfusion injury *in vivo*. Cancer cells with high basal AMPK activation are resistant to ferroptosis, and AMPK inactivation sensitizes these cells to ferroptosis. Functional and lipidomic analyses further link AMPK regulation of ferroptosis to AMPK-mediated phosphorylation of acetyl-CoA carboxylase (ACC) and polyunsaturated fatty acid biosynthesis. Together, our study demonstrates that energy stress inhibits ferroptosis partly through AMPK, and reveals an unexpected coupling between ferroptosis and AMPK-mediated energy stress signaling.

Keywords

ferroptosis; energy stress; glucose starvation; AMPK; lipid peroxidation

Introduction

Normal cells require an adequate supply of nutrients and energy to survive. Depletion of nutrients and energy induces metabolic stress[1]. One type of metabolic stress is energy stress, which is characterized by the depletion of intracellular ATP and a corresponding increase in intracellular AMP levels. Energy stress initially induces adaptive responses, which attempt to reestablish energy homeostasis. One important energy-stress-induced adaptive response is mediated by AMP-activated protein kinase (AMPK), a critical sensor of cellular energy status[2]. In response to energy stress, AMPK is activated via AMP binding, upstream kinase phosphorylation, and other mechanisms[2]. Once activated, AMPK phosphorylates a myriad of downstream targets to promote ATP-generating catabolic processes and inhibit ATP-consuming anabolic processes, thereby restoring energy balance and maintaining cell survival under conditions of energy stress[3]. However, under long-term and severe energy stress with excessive ATP depletion, such adaptive responses are unable to restore energy balance, and unresolved energy stress eventually induces apoptosis[1, 4, 5]. Whether energy stress regulates other non-apoptotic forms of regulated cell death remains largely unknown.

Ferroptosis is a non-apoptotic form of regulated cell death that is induced by overproduction of phospholipid hydroperoxides in an iron-dependent manner[6–10]. Ferroptotic cell death is not associated with apoptotic hallmarks, such as caspase-3 cleavage, can be induced in *BAX*/*BAK* deficient cells, and is suppressed by different inhibitors from those that block apoptosis or necroptosis; thus, ferroptosis is distinct from other forms of regulated cell death[6]. Dysregulation of ferroptosis is associated with various pathological conditions and human diseases, such as ischemia/reperfusion injury (IRI), neurodegeneration, and cancer[10–16].

Accumulating evidence indicates an intimate link between metabolism and ferroptosis[10, 17]. The antioxidant enzyme glutathione peroxidase 4 (GPX4) uses reduced glutathione (GSH) to convert phospholipid hydroperoxides to lipid alcohols and inhibits ferroptosis[18, 19]. GSH is synthesized from glutamate, cysteine, and glycine, among which cysteine is the rate-limiting precursor. Many cancer cells mainly obtain cysteine through the cystine-glutamate antiporter known as system x_c^--mediated transport of extracellular cystine, an oxidized

dimeric form of cysteine[10, 20]. Correspondingly, cystine depletion, inhibition of system x_c^--mediated cystine transport by erastin, or inactivation of GPX4 by RSL3 induces ferroptosis[6, 18]. How other metabolic processes or other forms of metabolic stress regulate ferroptosis remains less understood. In this study, we uncover a hitherto unrecognized coupling between energy stress and ferroptosis, with implications for the treatment of ferroptosis-associated diseases.

Results

Energy stress inhibits ferroptotic cell death.

Glucose provides the major energy source in most cells, and glucose starvation depletes ATP and induces energy stress. To study the role of energy stress in ferroptosis, we first examined the effect of glucose starvation on erastin-induced ferroptosis in immortalized mouse embryonic fibroblasts (MEFs). As expected, erastin treatment did not induce hallmarks of apoptosis, such as caspase-3 or PARP cleavage (Extended Data Fig. 1a), and erastin-induced cell death could be fully rescued by the ferroptosis inhibitor ferrostatin-1, the iron chelator deferoxamine (DFO), or the anti-oxidant N-acetyl-cysteine (NAC), but not by the apoptosis inhibitor Z-VAD-fmk or the necroptosis inhibitor necrostatin-1s (Extended Data Fig. 1b). Since glucose starvation is associated with ROS induction[21, 22] and ferroptosis is driven by lipid peroxidation[10], which is a type of ROS, we initially hypothesized that glucose starvation may potentiate erastin-induced ferroptosis. To our surprise, we observed that glucose starvation largely rescued erastin-induced ferroptosis in MEFs (Fig. 1a–b). Time course experiments (Extended Data Fig. 1c) revealed that erastin treatment induced almost complete cell death within 16–24 hours in immortalized MEFs, at which time points glucose starvation did not induce obvious cell death and almost completely rescued erastin-induced ferroptosis; the results are more difficult to interpret at later time points (48–96 hours) because glucose starvation alone also induced substantial cell death. Of note, glucose-starvation-induced cell death could not be blocked by ferrostatin-1 but was associated with caspase-3 cleavage (Extended Data Fig. 1c–d), suggesting that glucose starvation induced apoptosis but not ferroptosis in MEFs.

Ferroptosis can also be induced by cystine depletion (Extended Data Fig. 1e), GPX4 deletion or inactivation by its inhibitors, such as RSL3[18]. We found that ferroptosis induced by cystine depletion, RSL3 treatment, or GPX4 deletion were all significantly mitigated by glucose starvation (Fig. 1c–e). These data also suggested that glucose starvation likely impinges on the ferroptosis pathway downstream of GPX4, although we cannot completely rule out the possibility that glucose starvation might inhibit ferroptosis in parallel to or upstream of GPX4.

Further analysis in MEFs cultured in different concentrations of glucose revealed that ATP depletion correlated with the rescuing effects of glucose starvation on erastin-induced ferroptosis (Extended Data Fig. 1f–g). We further tested compounds that either induce or mimic energy stress, including 2-deoxy-glucose (2DG, a glucose analogue that blocks glycolysis), 5-aminoimidazole-4-carboxamide ribonucleotide (AICAR, an AMP analog), and A769662 (an AMPK activator). While treatment with these compounds alone did not induce significant cell death in immortalized MEFs, at least at the chosen concentrations and

time frames, they all significantly inhibited lipid peroxidation and ferroptosis induced by erastin, cystine depletion, or RSL3 treatment (Fig. 1f–k). We confirmed these findings in other cell lines, including Caki-1 and BJ cells (Extended Data Fig. 1h–k). Together, our results show that energy stress inhibits ferroptosis.

Energy stress inhibits ferroptotic cell death partly through AMPK.

Since all these treatments activate AMPK (Extended Data Fig. 1l), we tested whether AMPK is involved in energy-stress-mediated ferroptosis inhibition. Notably, *AMPK* double knockout (DKO) in MEFs almost completely reversed the inhibitory effect of glucose starvation, A769662, and 2DG on erastin-induced ferroptosis (Fig. 2a–c). It is known that defective AMPK signaling promotes energy-stress-induced cell death in MEFs[23–25]. It should be noted that there was no obvious cell death in *AMPK* DKO MEFs cultured in glucose-free medium or treated with A769662 or 2DG at the time points when erastin induced potent ferroptosis (Fig. 2b–c). However, at the time point for which erastin induced obvious ferroptosis, there was also substantial AICAR-induced cell death in *AMPK* DKO MEFs (Extended Data Fig. 1m), thus preventing us from examining the effect of *AMPK* deletion on AICAR-mediated ferroptosis inhibition. Of note, under treatment with 2 μM erastin, we did not observe any difference in erastin-induced ferroptosis between *AMPK* WT and DKO MEFs (Fig. 2b–c), likely because basal AMPK phosphorylation levels are low in MEFs (Fig. 2d); therefore, energy stress is needed to boost AMPK activity in order to reveal ferroptosis sensitivity differences between *AMPK* WT and DKO MEFs. Further dose-dependent analyses revealed that *AMPK* deletion promoted ferroptosis induced by low-dose erastin (0.25, 0.5, and 1 μM) in MEFs (Extended Data Fig. 1n).

We further correlated basal AMPK activation status (AMPK Thr172 phosphorylation under 25 mM glucose) with ferroptosis sensitivity in a panel of cell lines. We also examined SLC7A11 expression levels in these cell lines (*SLC7A11* encodes xCT, which is a critical component of system x_c^- [20]). Such analyses revealed that all SLC7A11-high cells were relatively more resistant to ferroptosis compared with SLC7A11-low cells (Fig. 2d–h). Notably, while AMPK activation status did not correlate with ferroptosis sensitivity in SLC7A11-high cells, we observed an inverse correlation between AMPK activation and ferroptosis sensitivity in SLC7A11-low cells (Fig. 2d–h). Together, these data suggest that energy stress inhibits ferroptosis at least partly through AMPK.

AMPK inactivation sensitizes cancer cells to ferroptotic cell death.

Our aforementioned data prompted us to further examine whether AMPK plays any causal role in ferroptosis resistance in the cell lines with high basal AMPK phosphorylation levels. We showed that inactivating AMPK by compound C dramatically sensitized ACHN cells (a ferroptosis-resistant cell line with high basal AMPK phosphorylation) to ferroptosis induced by erastin or cystine depletion (Fig. 3a–b, Extended Data Fig. 2a). Transmission electron microscopy (TEM) revealed that ACHN cells treated with compound C and erastin (or cystine depletion) exhibited shrunken mitochondria with increased membrane density, but did not show obvious DNA fragmentation in the nucleus, a characteristic morphologic feature of ferroptosis (Fig. 3c).

Overexpression of constitutively active (CA) AMPK (amino acids 1–312 of AMPK α1) in Caki-1 cells (a ferroptosis-sensitive cell line with low basal AMPK activation) moderately increased acetyl-CoA carboxylase (ACC) phosphorylation and partially protected cells from erastin-induced cell death (Fig. 3d–e). Conversely, *AMPKα1/α2* DKO in ACHN cells by CRISPR/Cas9 technology massively sensitized ACHN cells to ferroptosis induced by erastin, cystine depletion, or RSL3 (Fig. 2f–k, Extended Data Fig. 2b). We further showed that re-expression of AMPKα1, but not its T172A mutant or AMPKα2, in *AMPK* DKO ACHN cells restored AMPK and ACC phosphorylation (Fig. 3l), and largely rescued increased ferroptosis sensitivity in *AMPK* DKO cells (Fig. 3m), suggesting that AMPKα1 plays a dominant role in regulating ferroptosis in ACHN cells and that AMPK inhibits ferroptosis in a kinase-dependent manner. We subsequently confirmed our results in RCC4 cells, another ferroptosis-resistant cell line with high basal AMPK phosphorylation (Extended Data Fig. 2c–l). Finally, we showed that deletion of *LKB1*, the major upstream kinase of AMPK, also sensitized ACHN cells to ferroptosis (Extended Data Fig. 3a–b). Collectively, these results suggest that AMPK inhibits ferroptosis in cells with high basal AMPK activation.

AMPK-mediated ACC phosphorylation inhibits ferroptosis.

We next sought to study the underlying mechanism(s) by which energy-stress-mediated AMPK activation regulates ferroptosis. In response to energy stress, AMPK activates catabolic processes, particularly autophagy, and inactivates anabolic processes, most notably fatty acid synthesis and protein synthesis[2]. Since recent studies showed that autophagy promotes ferroptosis[26, 27], but our results show that energy-stress-mediated AMPK activation inhibits ferroptosis, it is less likely that AMPK inhibits ferroptosis through its activation of autophagy. AMPK inhibits protein synthesis through its inhibition of mechanistic target of rapamycin complex 1 (mTORC1)[23]. However, rapamycin treatment abolished mTORC1 activation (Extended Data Fig. 3c) but did not obviously affect erastin-induced ferroptosis (Extended Data Fig. 3d), suggesting that AMPK regulates ferroptosis likely through mTORC1-independent mechanisms. In addition, AMPK deficiency or its activation by AICAR or 2DG treatment did not significantly affect cystine uptake (Extended Data Fig. 3e–g) or cellular iron levels (Extended Data Fig. 3h).

ACC1 and ACC2 are two related enzymes that catalyze the synthesis of malonyl-CoA from acetyl-CoA, and function to promote fatty acid synthesis and inhibit fatty acid oxidation. Upon energy stress, AMPK inhibits fatty acid synthesis through its phosphorylation and inhibition of both ACC1 and ACC2[2]. We found that, similar to glucose starvation, treatment with 5-(tetradecyloxy)-2-furoic acid (TOFA), an allosteric inhibitor of ACC[28], potently inhibited lipid peroxidation (Fig. 4a–c) and ferroptosis (Fig. 4d–f, Extended Data Fig. 3i) induced by erastin, cystine depletion, or RSL3 in MEFs. Similar observations were made in other cell lines (Extended Data Fig. 3j–k). Consistently, metabolite profiling confirmed that, similar to glucose starvation or AICAR treatment, TOFA treatment decreased the levels of various fatty acids such as palmitic acid (C16:0) (Extended Data Fig. 3l–m). Importantly, TOFA treatment significantly mitigated increased lipid peroxidation and ferroptosis sensitivity in *AMPK* DKO ACHN cells (Fig. 4g–h), suggesting that ACC is a key downstream effector of AMPK in regulating ferroptosis.

We next studied whether AMPK-mediated ACC phosphorylation plays a role in ferroptosis inhibition by energy stress. To this end, we generated MEFs from *ACC* knock-in (KI) mouse model in which AMPK phosphorylation sites on both ACC1 (Ser79) and ACC2 (Ser212) were mutated to alanine (*ACC* DKI) (Fig. 4i)[29, 30]. Similar to *AMPK* deficiency (Fig. 2a–c), mutation of AMPK phosphorylation sites on ACC largely blocked the inhibitory effect of A769662, AICAR, or glucose starvation on erastin-induced ferroptosis (Fig. 4j–l). Together, our data strongly suggest that AMPK regulates ferroptosis at least partly through AMPK-mediated phosphorylation of ACC.

AMPK regulates PUFA generation.

The aforementioned data prompted us to characterize lipid profile alterations caused by AMPK activation or inactivation. To study the impact of AMPK activation on lipid metabolism, we performed untargeted lipidomic analyses in MEFs with treatment of vehicle (control), A769662, erastin, or A769662 + erastin (Extended Data Fig. 4a). As shown in Fig. 5a, A769662 treatment caused significant decreases (FDR-corrected p-value < 0.05, fold change > 1.5) in the levels of 64 lipid species compared with vehicle treatment. To examine the impact of AMPK deficiency on lipid metabolism, we also performed untargeted lipidomic analysis in *AMPK* WT and DKO ACHN cells with vehicle or erastin treatment (Extended Data Fig. 4b). As shown in Fig. 5b, we observed significant increases (FDR-corrected p-value < 0.05, fold change > 1.5) in the relative abundance of 73 lipid species in *AMPK* DKO ACHN cells compared with WT ACHN cells (under vehicle treatment). Consistent with previous reports[31, 32], erastin treatment altered the levels of several lipid species in both analyses; importantly, A769662 treatment (or *AMPK* deletion) exerted similar global effects on lipid profiles under conditions of both vehicle and erastin treatment (Extended Data Fig. 4c–d).

By integrating the data sets from these two analyses, we identified 17 lipid species that were downregulated by A769662 treatment in MEFs but upregulated by *AMPK* deletion in ACHN cells) (Fig. 5c and Extended Data Fig. 5a), including PUFAs such as dihomo-γ-linolenic acid (C20:3) and arachidonic acid (C20:4) (Fig. 5d–e). Further analyses confirmed that other FAs, such as palmitic acid (C16:0) and adrenic acid (C22:4), were similarly altered by AMPK activation or inactivation (although the fold changes did not meet the 1.5-fold cutoff under one or the other condition) (Extended Data Fig. 5b–c).

Accumulation of oxygenated phosphatidylethanolamines (PEs), specifically arachidonic acid (C20:4)- and adrenic acid (C22:4)-containing PEs, are believed to play direct roles in driving ferroptosis[33]. Consistent with this, our lipidomic analyses showed that A769662 treatment decreased, whereas *AMPK* deletion increased the levels of PE 18:0_20:4 and PE 18:0_22:4 (Extended Data Fig. 6a–b). ACSL4-mediated PUFA-containing PE biosynthesis has been shown to be critical in driving ferroptosis[31, 33, 34]. We showed that ACSL4 deletion largely blocked erastin-induced ferroptosis in *AMPK* DKO cells (Extended Data Fig. 6c–d). Supplementation of γ-linolenic acid (a precursor for dihomo-γ-linolenic acid synthesis) and arachidonic acid significantly sensitized A769662-treated MEFs or *AMPK* WT ACHN cells to erastin-induced ferroptosis (Fig. 5f–g). We confirmed that supplementation of dihomo-γ-linolenic acid or arachidonic acid increased the levels of pro-ferroptotic PE 18:0_22:4 (and

arachidonic acid treatment also increased the levels of PE 18:0_20:4) (Extended Data Fig. 6e–f). Finally, we showed that supplementation of palmitic acid and stearic acid, the two most proximal fatty acids to AMPK, also sensitized ACHN cells to erastin-induced ferroptosis (Extended Data Fig. 6g–h).

To further substantiate our observations, we conducted untargeted lipidomic analysis in MEFs treated with TOFA (with or without erastin treatment). We observed significant changes (one-way ANOVA, FDR-corrected p-value < 0.05) in the relative abundance of many lipid species, including decreasing palmitic acid and palmitoleic acid levels, upon TOFA treatment (Extended Data Fig. 6i–j). Of note, TOFA and A769662 treatments exhibited somewhat different lipidomic profiles (Extended Data Fig. 4c and Extended Data Fig. 6i). This is not entirely surprising, considering that AMPK activation by A769662 would also modulate other lipid metabolic enzymes besides inactivating ACC. Notably, A769662 and TOFA decreased the levels of the same PUFA-containing PEs, including PE 18:0_22:4, PE 18:1_22:6, PE 16:0_22:6, PE P-18:1_22:6, PE P-18:0_22:6 and TAGs (Extended Data Fig. 7a–d), which is consistent with the current model that it is the oxidation of PUFA-containing PEs that drives ferroptosis[33]. Together, these lipidomic analyses suggest that AMPK activation suppresses whereas AMPK deficiency drives PUFA-containing lipid biosynthesis, thus altering cellular sensitivity to ferroptosis.

Energy-stress-induced AMPK activation inhibits renal IRI.

Our findings from cell line studies prompted further analysis of AMPK function in ferroptosis-associated pathological conditions *in vivo*. Consistent whith previous studies which indicated a role of ferroptosis in renal IRI[13, 19], TEM analysis revealed a striking ferroptosis-associated morphologic change in renal epithelial cells upon renal IRI characterized by smaller mitochondria with increased membrane density (Fig. 6a). To examine whether energy stress inducers, by inhibiting ferroptosis, would protect renal IRI, we treated WT mice with vehicle, AICAR, 2DG, or ferrostatin-1 (as a positive control), and then subjected the mice to an established renal IRI protocol[13]. As expected, AICAR or 2DG treatment significantly increased AMPK phosphorylation in kidneys (Fig. 6b). Consistent with previous findings[13], ferrostatin-1 treatment partially protected mice from renal IRI as quantified by tubular damage in renal cortex (characterized by tubular dilatation, tubule brush border loss, flattened epithelial cells, or sloughing of cells); notably, AICAR or 2DG treatment exhibited a similar protective effect on renal IRI as did ferrostatin-1 (Fig. 6c–d).

To study the potential role of AMPK in renal IRI, we generated *AMPKα1/α2*$^{L/L}$*, Rosa26-CreERT2* mouse model. Tamoxifen treatment significantly decreased AMPK levels in kidneys of *AMPKα1/α2*$^{L/L}$*, Rosa26-CreERT2* (hereafter referred to as *AMPK* DKO) mice compared with those in *AMPKα1/α2*$^{L/L}$ control (hereafter referred to as *AMPK* WT) mice (Extended Data Fig. 8a). Consistent with a recent report using the same mouse model[35], *AMPK* DKO mice maintained normal body weight at least within 2 months after tamoxifen treatment, and did not show obvious phenotypic differences in kidneys before or after IRI compared with WT controls (Extended Data Fig. 8b). Similar to our observations made in MEFs (see Fig. 2a–c), we found that AICAR-mediated protective effect on renal IRI-induced renal damage and blood urea nitrogen (BUN) levels was largely abolished in *AMPK*

DKO mice (Fig. 6e–g). Immunohistochemical analysis of 4-hydroxy-2-noneal (4-HNE, a lipid peroxidation marker) revealed that 4-HNE staining significantly overlapped with tubular damage in renal cortex upon IR (Extended Data Fig. 8c). *AMPK* deletion did not affect IR-induced 4-HNE staining in kidneys in vehicle-treated mice but suppressed the protective effects of AICAR treatment to reduce 4-HNE staining (Fig. 6h–i). This observation was further confirmed with immunohistochemical analysis of malondialdehyde, another lipid peroxidation marker (Extended Data Fig. 8d–e). Together, these *in vivo* data strongly suggest that energy stress exerts a protective effect on renal IRI at least partly through AMPK activation, which potentially relates to energy-stress-mediated inhibitory effect on lipid peroxidation and ferroptosis. It should be noted that a protective role of AMPK in regulating renal IRI has also been described in previous studies, possibly via AMPK-mediated autophagy activation[36, 37]. Our study further suggests that AMPK may regulate renal IRI through ferroptosis.

Discussion

Glucose is the principal nutrient to maintain biosynthetic, bioenergetic, and redox homeostasis and to maintain cell survival in most cells[38]. Glucose starvation leads to cell death dues to ROS induction and/or energy depletion[4, 22]. Because ferroptosis is induced by lipid peroxidation, a ROS-mediated lipid damage, it appears logical that, if any, glucose starvation should promote ferroptosis. In this study, we revealed a counterintuitive finding that glucose is required for ferroptosis and that glucose starvation largely prevents cells from undergoing ferroptosis. We found that treatments that induce or mimic energy stress inhibit ferroptosis *in vitro* or ferroptosis-associated renal IRI *in vivo* at least partly through AMPK activation. Under these conditions with low basal AMPK activation, boosting AMPK activation by energy stress inhibits ferroptosis. Conversely, in ferroptosis-resistant cell lines with high basal AMPK activation, AMPK inactivation dramatically sensitizes these cells to ferroptosis. Collectively, our study convincingly establishes an inhibitory role of AMPK in regulating ferroptosis, and further suggests that AMPK activators may be useful to treat the diseases or pathological conditions induced by ferroptosis, such as IRI. Mechanistically, our data suggest that the inhibitory effects of AMPK activation on ferroptosis does not involve modulation of autophagy, mTORC1 signaling, cystine uptake, or iron metabolism. Instead, our data support a model wherein energy stress activates AMPK and AMPK then phosphorylates and inactivates ACC, resulting in restrained biosynthesis of PUFAs and other fatty acids, and ferroptosis inhibition (Extended Data Fig. 9).

A recent study showed that mitochondria play an important role in regulating ferroptosis[39]. AMPK is also vital for regulating mitochondrial homeostasis[40]. However, we would like to note a major difference between mitochondria and AMPK function in ferroptosis. While mitochondria selectively promote cystine-starvation-induced or erastin-induced, but not RSL3-induced, ferroptosis[39], our data clearly showed that glucose starvation or *AMPK* deficiency affects ferroptosis induced by all these ferroptosis inducers. Therefore, our data suggest that energy-stress-mediated AMPK activation inhibits ferroptosis likely through mitochondria-independent mechanisms. Furthermore, since lipid metabolism, particularly PUFA biosynthesis, is important for ferroptosis mediated by different ferroptosis inducers[31, 33, 34], our proposed model linking AMPK-mediated lipid metabolism to

ferroptosis is in line with the data that *AMPK* deficiency sensitizes cells to all ferroptosis inducers we have tested.

A recent study also reported a promoting role of AMPK in regulating ferroptosis[41], which is opposite to our findings described here. We would like to point out several discrepancies between these studies. First, in contrast to this study, we did not observe any major effect of erastin on AMPK or ACC phosphorylation in the cell lines we have examined (Extended Data Fig. 2a). In addition, while this study proposed that AMPK-mediated BECN1 phosphorylation promotes ferroptosis by inhibiting SLC7A11-mediated cystine transport, we found that AMPK deletion or its activation by AICAR or 2DG treatment did not significantly affect cystine uptake (Extended Data Fig. 3e–g). It is possible that AMPK function in regulating ferroptosis is context dependent, which awaits further investigations in future studies.

We and others previously showed that ferroptosis is also an important tumor suppression mechanism[11, 14, 42–45]. Although ferroptosis has been linked to multiple pathological conditions or diseases, its physiological function still remains enigmatic. We propose that tumor suppression may represent one physiological function of this form of regulated cell death. Our current study linking AMPK to ferroptosis also raises an intriguing question on whether AMPK regulation of ferroptosis plays a role in tumor biology. The exact role of AMPK in tumor biology is highly context dependent. AMPK can exert either a tumor-suppressive function by inhibiting major biosynthetic pathways (such as protein or fatty acid biosynthesis) or a tumor-promoting function by promoting tumor cell survival under metabolic stress conditions[46]. While the tumor-suppressive role of the AMPK pathway is well established[47], multiple recent studies have also convincingly established a tumor-promoting role of AMPK in some tumor types[35, 48–51]; in addition, some isoforms of AMPK are overexpressed or amplified in certain cancers[52]. In light of our current data showing that AMPK inhibits ferroptosis, it is tempting to speculate that AMPK's pro-tumorigenic function might be at least partly mediated through its inhibition of ferroptosis in some contexts. Future studies will be directed to further dissect the potential role of ferroptosis in AMPK-mediated tumor development.

Methods

Mice

All animal experiments were performed in accordance with a protocol approved by the Institutional Animal Care and Use Committee (IACUC) of The University of Texas MD Anderson Cancer Center; the protocol is in full compliance with policies of the Institutional Animal Care and Use Committee. *AMPKα1/α2*$^{L/L}$ mice were provided by Dr. Daisuke Nakada[48] and crossed with *Rosa26-CreERT2* mice as described in our previous publications[53, 54]. Five-week-old mice were intraperitoneally injected with tamoxifen (Sigma-Aldrich, 120 μg/g body weight) for five consecutive days. Mice were subjected to IRI at two weeks post tamoxifen injection. For AICAR (Toronto Research Chemicals) or 2DG (Sigma-Aldrich) treatment, mice were either injected with vehicle (PBS) or drugs (0.5 mg/g) at ten days after the last tamoxifen injection for seven days. Then, IRI was performed on the next day. Ferrostatin-1 (Sigma-Aldrich) was injected 30 min prior to IRI. All mouse

injections were intraperitoneal, and the doses were calculated according to mouse body weight.

Primary cells

Primary mouse embryonic fibroblasts (MEFs) were established from embryos at E13.5 as previously described[55]. MEFs were cultured in Dulbecco's modified Eagle's medium (DMEM) with 10% fetal bovine serum (FBS) and 1% penicillin/streptomycin at 37°C incubator with humidified atmosphere of 20% O_2 and 5% CO_2. The primary MEFs were immortalized by infection of SV40 large T antigen (LT-MEFs). To generate *AMPK* α1/α2 WT and DKO MEFs, *AMPKα1/α2*$^{L/L}$ LT-MEFs were infected with either empty vector control (pBABE-EV) or Cre-recombinase-expressing retrovirus (pBABE-Cre) and selected with puromycin (2 μg/ml) for four days. Immortalized *ACC* WT and DKI MEFs were previously described[29].

Cancer cell lines

BJ, ACHN, Caki-1, A498, MCF7, MDA-MB-231, A375, and A549 cell lines were obtained from ATCC. RCC4 and UMRC6 cell lines were obtained from Dr. William G. Kaelin at Dana-Farber Cancer Institute. PANC-1 and DanG cell lines were obtained from Dr. Haoqiang Ying at MD Anderson Cancer Center. H157 cell line was obtained from Dr. Jack A. Roth at MD Anderson Cancer Center. All cell lines were cultured in culture media supplemented with 10% (v/v) fetal bovine serum and 1% (v/v) penicillin/streptomycin at 37°C incubator with a humidified atmosphere of 20% O_2 and 5% CO_2. RCC4, PANC-1, A549, MDA-MB-231, DanG, UMRC6, and A375 cell lines were cultured in Dulbecco's modified Eagle's medium (Sigma, D6429). BJ, ACHN, MCF7, and A498 cell lines were cultured in Eagle's Minimum Essential Medium (ATCC, 30–2003). H157 cell line was cultured in RPMI-1640 medium (Sigma, R8758) and Caki-1 cell line was cultured in McCoy's 5a Medium Modified (ATCC, 30–2007).

All cell lines were cultured in a 10 cm plate and subcultured into a 12-well plate for cell death and lipid peroxidation measurement. For cell viability assay, cells were subcultured into a 96-well plate. Cells were treated with ferroptosis inducers, erastin (EMD Millipore), or RSL3 (Selleckchem); apoptosis inducer, staurosporine (LC Laboratories); cell death inhibitors, ferrostatin-1 (Sigma-Aldrich), necrostatin-1s (BioVision), or Z-VAD-fmk (R&D Systems); antioxidant, N-acetyl cysteine (NAC, Sigma-Aldrich); iron chelator, deferoxamine (Sigma-Aldrich); AMPK activator/inhibitors, A769662 (LC Laboratories), 5-Aminoimidazole-4-carboxamide ribonucleotide (AICAR, Toronto Research Chemicals), 2-deoxy-D-glucose (2DG, Sigma-Aldrich), compound C (Sigma-Aldrich); acetyl-coA carboxylase inhibitor, TOFA (Millipore). For glucose-free media and cystine-free media treatment, cells were cultured in normal growth media, and then subcultured into 12-well plates. After overnight culture, cells were washed twice with PBS and the media was replaced with glucose- or cysteine-free media. Dialyzed FBS was used for glucose-free and cystine-free media.

Plasmid constructs

The gateway donor vectors containing AMPK α1 wild-type and T172A mutant were described in our previous publications[25, 56]. These genes were integrated into pLenti6.3/V5 destination vector (Invitrogen) using gateway cloning. The sequences were verified from single clones. The pLeinti-CMV/TO_PRKAA2 (AMPK α2) was obtained from Addgene (Plasmid #74447). The constitutively active (CA) AMPK (amino acids 1–312 of AMPK α1) construct was described in our previous publication[25].

CRISPR/Cas9-mediated gene knockout

Knockout of *AMPK* α1/α2, *LKB1*, *GPX4* and *ACSL4* in human cell lines was performed using single guide RNAs (sgRNAs) and CRISPR/Cas9 technology. sgRNAs were cloned into the lentiviral lentiCRISPR v2 vector or transient expression vector, pSpCas9(BB)-2A-GFP (PX458). sgAMPK α1: 'CCAGGAACTGA GTCTGCGCA', 'CTCACCCTTCACTTTGCCGA', 'TACTC AATCGACAGAAGATT'; sgAMPK α2: 'GAAGATCGGACACTACGTGC', 'GTTGGAGAAC ATCAATTAAC', 'ACTTACAGTTTGATAATATG'; sgLKB1: 'CCCTGGGTCCAGCATGGA GG', 'CACGGAGGGCGAGCTGATGT', 'AGCTTGGCCCGCTTGCGGCG'; sgGPX4: 'GAG ATCAAAGAGTTCGCCGC '; sgACSL4: 'AATAAAGCAGAGTACCCTGA', 'GAAGGCGTT GGTCTACTTGG'. lentiCRISPR v2 clones were transfected into HEK293T cells with psPAX2 packaging plasmid and pMD2.G VSV-G envelope expressing plasmid. ACHN cells were infected with lentivirus with 0.8 μg/ml of polybrene, selected with puromycin (2 μg/ml, Invivogen) for three days, and single cells were sorted into 96-well plates. For transient transfection of PX458-guide RNA clones, SF Cell Line 4D-Nucleofector X kit (Lonza) was used according to the manufacturer's protocol. Briefly, 2 X 10^5 ACHN cells mixed with 1 μg of plasmid, nucleofector solution, and supplement were subjected to nucleofection using a 4D-Nucleofector core unit. 24 h after the transfection, GFP positive single cells were sorted into 96-well plates. Single cells were maintained in Eagle's Minimum Essential Medium (ATCC, 30–2003) with 10% (v/v) fetal bovine serum and 1% (v/v) penicillin/streptomycin at 37°C incubator with 5% CO_2 for 3–4 weeks and each colony was verified by western blot and DNA sequencing to confirm the target gene deletion. To enhance the gene silencing efficiency, we also used the construct with doxycycline (DOX)-inducible Cas9 expression, which was kindly provided by Dr. Westbrook (Baylor College of Medicine). ACHN cells were infected with lentivirus carrying the DOX-inducible Cas9 and selected with 400 μg/ml of G418 (Sigma-Aldrich). 1 μg/ml of doxycycline (Sigma-Aldrich) was added into the media 48 h prior to PX458-guide RNA infection, and cells were then cultured in DOX free media 24 h after the sgRNA infection.

To generate *GPX4* KO cells, doxycycline (DOX)-inducible Cas9 expressing Caki-1 cells were infected with sgRNAs targeting GPX4. Doxycycline was added into the media in the presence of 1 μM of ferrostatin-1. Cells were cultured with standard cell culture media supplemented with 1 μM of ferrostatin-1. For inducing ferroptosis, ferrostatin-1 was removed from media.

Cell death assays

Cell death was measured by propidium iodide (PI, Roche) staining using a flow cytometer as previously described[57, 58]. For PI-staining, cells were seeded at a density of 70–80% confluence into 12-well plates. Next day, cells were treated with different reagents and media. To measure the cell death, cells were collected including floating dead cells, stained with 5 μg/ml PI (Sigma) and the percentage of PI-positive dead cell population was analyzed by the flow cytometer, BD Accuri C6 (BD Biosciences) using a FL2 detector. Minimum of 5,000 single cells were analyzed per well and all experiments were carried out at least in triplicate. For cells treated simultaneously with ferroptosis inducers and energy stress inducers, appropriate times were selected to analyze cell death/lipid peroxidation before the lethal effect by energy stress inducers.

Cell viability assay

Viable cells were measured using Cell Counting Kit-8 (CCK-8, Dojindo) as previously described[59, 60]. Briefly, ACHN cells were seeded onto 96-well plates at a density of 2 X 10^4/well. Next day, cells were treated with fatty acids for 24 h. Subsequently, cells were treated with erastin or left untreated for 16 h and then exposed to 10 μl of CCK-8 reagent (100μl medium/well) for 1 h at 37°C, 5% CO_2 incubator. The absorbance at a wavelength of 450 nm was determined using a FLUOstar Omega micro plate reader (BMG Labtech).

Determination of lipid peroxidation

Cells were seeded on 12-well plates and incubated overnight. On the next day, cells were treated with compounds for the indicated times, harvested by trypsinization and resuspended in 200 μl PBS containing 5 μM of C11-BODIPY 581/591 (Invitrogen). Cells were incubated for 30 min at 37°C in a water bath. Lipid peroxidation was assessed by flow cytometer, BD Accuri C6 using a 488 nm laser on a FL1 detector. Minimum 5,000 single cells were analyzed per well.

Intracellular ATP level measurement

Intracellular ATP levels were measured by CellTiter-Glo® Luminescent assay kit (Promega, G7570) according to manufacturer's instruction and as previously described[61]. Briefly, 10000 cells/well were seeded in a 96-well plate one day before treatment. After cells were cultured in medium with different glucose concentrations as indicated, each well was added with 100 μl CellTiter-Glo® Reagent and incubated for 10 min at room temperature on a shaker. Then luminescence of each well was subsequently measured with a Gen5 microplate reader (BIOTEK).

Fatty acid-dependent sensitization of ferroptosis

MEFs and ACHN cells were plated onto 96-well plates at a density of 1 X 10^4/well (MEFs) and 2 X 10^4/well (ACHN). After overnight incubation, cells were treated with specified fatty acids or fatty acids + 1 μM Ferrostatin-1 with a series of fatty acid concentration ranging from 40 μM to 0 μM for 24 h. Subsequently, cells were treated simultaneously with fatty acids with or without 2 μM erastin for 12 h (MEFs) and 18 h (ACHN), and cell viability was evaluated using CCK-8 reagent.

Cystine uptake assay

Cystine uptake assay was conducted as previously described[14]. Briefly, cells were plated in 12-well plates and incubated overnight. To measure the cysteine uptake, the medium was replaced with fresh DMEM (which contains 200 μM Cystine) containing [^{14}C] Cystine (PerkinElmer, 0.04 μCi), and cells were incubated for 2 h or 4 h. For Extended Data Fig. 3f–g, cells were pre-treated with AICAR or 2DG for 4 h and [^{14}C] Cystine was added into media for additional 2 h. Uptake was terminated by rapidly rinsing cells twice with cold PBS and lysed in 0.1 mM NaOH. Radioactivity (DPM, disintegrations per minute) was measured using Tri-Carb Liquid Scintillation Analyzer (PerkinElmer, 4810TR) in the presence of quench curve. All experiments were carried out in triplicate.

Labile iron pool measurement

ACHN cells were seeded into 12-well plates at a density of 2 X 10^5 per well. On the next day, cells were incubated with 20 nM of Calcein-AM (C3099, Invitrogen) for 15 min and washed with PBS. Cells were then harvested and analyzed by flow cytometer, BD Accuri C6 using a 488 nm laser on a FL1 detector.

Immunoblotting

Western blotting to analyze protein expression was performed as previously described[62–64]. Briefly, cell pellets and tissues were lysed using RIPA lysis buffer (Millipore) and the protein concentration was determined by a Bradford assay (Bio-Rad) using a Nanodrop2000 (Thermo scientific). 15–20 μg of protein was used for immunoblot analysis using antibodies against phospho-AMPKα (Thr172, 1:1000, 2535, Cell Signaling), AMPKα (1:1000, 5832, Cell Signaling) AMPK α1 (1:1000, 2795, Cell Signaling), AMPKα2 (1:1000, 2757, Cell Signaling), phospho-ACC (S79, 3661, 1:1000, Cell Signaling), ACC (1:1000, 3662, Cell Signaling), phospho-S6 (Ser240/244, 1:5000, 3661, Cell Signaling), S6 (1:1000, 2217, Cell Signaling), phospho-S6K (Thr389, 1:1000, 9205, Cell Signaling), S6K (1:1000, sc-230, Santa Cruz), phospho-ULK1 (S757, 6888, 1:1000, Cell Signaling), ULK1 (1:1000, 8054, Cell Signaling), LKB1 (1:1000, sc-32245, Santa Cruz), SLC7A11 (1:3000, 12691, Cell Signaling), GPX4 (1:1000, MAB5457, R&D systems), ACSL4 (1:1000, sc-271800, Santa Cruz), Cleaved Caspase-3 (Asp175, 1:500, 9661, Cell Signaling), Cleaved-PARP (Asp214, 1:1000, 9544, Cell Signaling), Vinculin (1:50000, V4505, Sigma).

Histology, analysis of organ damage, and immunohistochemistry

Fresh kidney tissues were fixed in 10% neutral buffered formalin overnight, washed once with PBS, and stored in 70% ethanol at 4°C. The tissues were dehydrated and embedded in paraffin by Research Histology Core Laboratory (MD Anderson Cancer Center) according to standard protocols. Embedded tissues were sectioned at a thickness of 5 μm for hematoxylin & eosin (H&E), 4-HNE and MDA staining. H&E stained kidney sections were analyzed using an Olympus BX43 microscope. Organ damage on the renal cortex was evaluated by the following parameters: tubular dilatation, tubule blush border loss, flattened epithelial cells, and sloughing of cells. The primary antibodies, 4-HNE (ab46545, Abcam, 1:200) or MDA (JAI-MMD-030N, Adipogen, 1:100), were incubated overnight at 4°C. Staining was performed using the Vectastain elite ABC kit and DAB peroxidase substrate kit

(Vector laboratories). Images were randomly taken from the renal cortex (10 images per mouse) at 200 X magnification using an Olympus BX43 microscope, and the percentage of 4-HNE positive tubular cells per image was analyzed.

Kidney ischemia-reperfusion injury

Induction of kidney IRI was performed via the dorsal approach and a bilateral renal pedicle clamping for 30 min. Mice were anesthetized with an intraperitoneal injection of Ketamine (100 mg/kg, Henry Schein) /Xylazine (10 mg/kg, Sigma) and an analgesics, sustained-release Buprenorphine (ZooPharm) was injected subcutaneously. Throughout the surgical procedure, heating pads were used to maintain the mouse body temperature. Via dorsal approach, the right kidney was removed and the left renal pedicle was clamped for 30 min using a vascular clamp. The muscle layer and skin layer were closed using 5–0 vicryl sutures (Ethicon). Sham-operated mice underwent identical surgical procedures, except the renal pedicle clamping. All mice were sacrificed 24 h after reperfusion. In some experiments, AICAR (0.5 mg/g) and 2DG (0.5 mg/g) were injected into mice for seven days before IRI, and the surgical procedure was performed on the next day of the last AICAR/2DG injection. For ferrostatin-1 treatment, mice were injected with 200 μl of PBS for 7 days and 2 μg/g of ferrostatin-1 was injected into the mice 30 min prior to ischemia. For TEM analysis, the fresh kidneys were cut into slices perpendicular to the long axis from the renal cortex and $1mm^3$ cubes were fixed at 4°C using the solution provided by the High-Resolution Electron Microscopy Facility at MD Anderson Cancer Center.

Transmission electron microscopy (TEM)

TEM analysis was performed by the High Resolution Electron Microscopy facility at MD Anderson Cancer Center. Samples were fixed with a solution containing 3% glutaraldehyde plus 2% paraformaldehyde in 0.1 M cacodylate buffer, pH 7.3, then washed in 0.1 M sodium cacodylate buffer and treated with 0.1% Millipore-filtered cacodylate buffered tannic acid, postfixed with 1% buffered osmium, and stained en bloc with 1% Millipore-filtered uranyl acetate. The samples were dehydrated in increasing concentrations of ethanol, infiltrated, and embedded in LX-112 medium. The samples were polymerized in a 60°C oven for approximately 3 days. Ultrathin sections were cut in a Leica Ultracut microtome (Leica, Deerfield, IL), stained with uranyl acetate and lead citrate in a Leica EM Stainer, and examined in a JEM 1010 transmission electron microscope (JEOL, USA, Inc., Peabody, MA) at an accelerating voltage of 80 kV. Digital images were obtained using the AMT Imaging System (Advanced Microscopy Techniques Corp, Danvers, MA).

Lipidomic analyses

Sample preparation. Lipids were extracted from each cell pellet using a modified Matyash[65] method as described previously[66]. Briefly, MEFs cells were cultured in 0 mM glucose containing media or treated with vehicle (DMSO), 2 mM AICAR, 200 μM A769662, 25 μM TOFA, 2 μM erastin, 200 μM A769662 + 2 μM erastin, or 25 μM TOFA + 2 μM erastin for 8 hours. *AMPK* WT and DKO ACHN cells were treated with vehicle (DMSO) or 2 μM erastin for 11 hours. In addition, ACHN cells were treated with vehicle (DMSO), 20 μM dihomo-γ-linolenic acid or 20 μM arachidonic acid for 18 hours. For

Extended Data Fig. 3m, the frozen cell pellets were processed and analysed by Mayo Clinic Hospital metabolomics core, Rochester, MN. All the other lipidomic analyses were performed as follows. Cells were homogenized in 250 μL cold methanol containing 0.01% butylated hydroxytoluene (BHT) and 1 μl of SPLASH lipidomics internal standard mix (Avanti Polar Lipids, INC.) with microtip solicitor. Homogenized samples were transferred to fresh glass vials containing 850 μL of cold methyl-tert-butyl ether (MTBE) and vortex-mixed for 30 sec. To enhance the extraction efficiency of lipids, the samples were incubated on ice for 2 hours on the shaker. After the addition of 200 μL of ice-cold water, the samples were incubated for 20 min on ice and centrifuged at 3,000 rpm for 20 min at 4°C. The upper phase containing the lipids were collected and dried down under a gentle stream of nitrogen gas. The dried samples were reconstituted with 2-propanol/ acetonitrile /water (4:3:1; v/v/v and 0.01% BHT) before LC-MS analysis. A quality control (QC) sample was prepared by combining 40 μL of each sample to assess the reproducibility of the features through the runs. **LC conditions**. Lipids were separated using an Acquity UPLC HSS T3 column (2.1×100 mm, 1.8 μm) over a 17 min gradient elution on Waters Acquity UPLC I-Class system. Mobile phase A was consisted of acetonitrile/water (60:40, v/v) and mobile phase B was 2-propanol/acetonitrile/water (85:10:5, v/v/v) both containing 10 mM ammonium acetate and 0.1% acetic acid. The gradient profile was 40% B for 1.5 min, 40–100% B in 10.5 min, 100% B for 3 min, 40% B in 1 min, and 40% B for 1 min. The oven temperature was set at 55°C, and the flow rate was 400 μL/min. The injection volume was 6 μL using the flow-through needle mode. The QC sample was injected between the samples, at the beginning and end of the run to monitor the performance and the stability of the MS platform. **MS conditions**. The SYNAPT G2-Q-ToF mass spectrometer was operated in both positive and negative electrospray ionization (ESI) modes. For positive mode, a capillary voltage and sampling cone voltage of 3 kV and 32 V were used. The source and desolvation temperature were kept at 120°C and 500°C, respectively. Nitrogen was used as desolvation gas with a flow rate of 900 L/hr. For negative mode, a capillary voltage of 2 kV and a cone voltage of 30 V were used. The source temperature was 120°C, and the desolvation gas flow was set to 850 L/hr. Dependent on the ionization mode the protonated molecular ion of leucine encephalin ($[M+H]^+$, m/z 556.2771) or the deprotonated molecular ion ($[M-H]^-$, m/z 554.2615) was used as a lock mass for mass accuracy and reproducibility. The data were collected in duplicates in data independent (MS^E) mode over the mass range m/*z* 50 to 1600 Da. The QC sample was also acquired in enhanced data-independent ion mobility (HDMSE) in both positive and negative modes for enhancing the structural assignment of lipid species. The ESI source settings for ion mobility were the same as described above. The traveling wave velocity was set to 650 m/s and wave height was 40 V. The helium gas flow in the helium cell region of the ion-mobility spectrometry (IMS) cell was set to 180 mL/min. Nitrogen as the drift gas was held at a flow rate of 90 mL/min in the IMS cell. The low collision energy was set to 4 eV, and high collision energy was ramping from 25 to 65 eV in the transfer region of the T-Wave device to induce fragmentation of mobility-separated precursor ions. **Data pre-processing and statistical analysis**. All raw data files were converted to netCDF format using DataBridge tool implemented in MassLynx software (Waters, version 4.1). Then, the data were subjected to peak-picking, retention time alignment, and grouping using "XCMS"[67, 68] package (version 3.0.2) in R (version 3.4.4) environment. After retention time alignment and filling missing peaks, an output data frame

was generated including the list of time-aligned detected lipid features (m/z and retention time) and the relative signal intensity (area of the chromatographic peak) in each sample. Multivariate and univariate statistical analyses were performed using MetaboAnalyst[69] (version 4.0) and also in R environment. Group differences were calculated using either a two-tailed parametric Welch's t-test with fold change threshold of 1.5 (Average signal intensities of treated over average signal intensities of vehicle groups), or one-way ANOVA. P-values were corrected for multiple hypothesis testing and a false discovery rate (FDR) of 0.05 or less was considered significant. **Structural assignment of identified lipids**. Structural elucidation and validation of significant features were initially obtained by searching monoisotopic masses against the available online databases such as METLIN, Lipid MAPS, and HMDB with a mass tolerance of 5 ppm. Fragment ion information obtained by tandem MS (UPLC-HDMSE) was utilized for further structural elucidation of significantly changed lipid species. HDMSE data were processed using MS^E data viewer (Version 1.3, Waters Corp., MA, USA).

Statistics and reproducibility

All experiments were independently repeated more than two times with similar results. Statistical analyses (unpaired, two-tailed t-test) shown in bar plots were performed with GraphPad Prism 8 software using a two-tailed t-test. The data are presented as means ± SD of three biologically independent experiments or samples. For lipidomics analysis in Extended Data Fig. 4c, d, one-way analysis of variance (ANOVA) was performed. A P value less than 0.05 was considered significant.

Extended Data

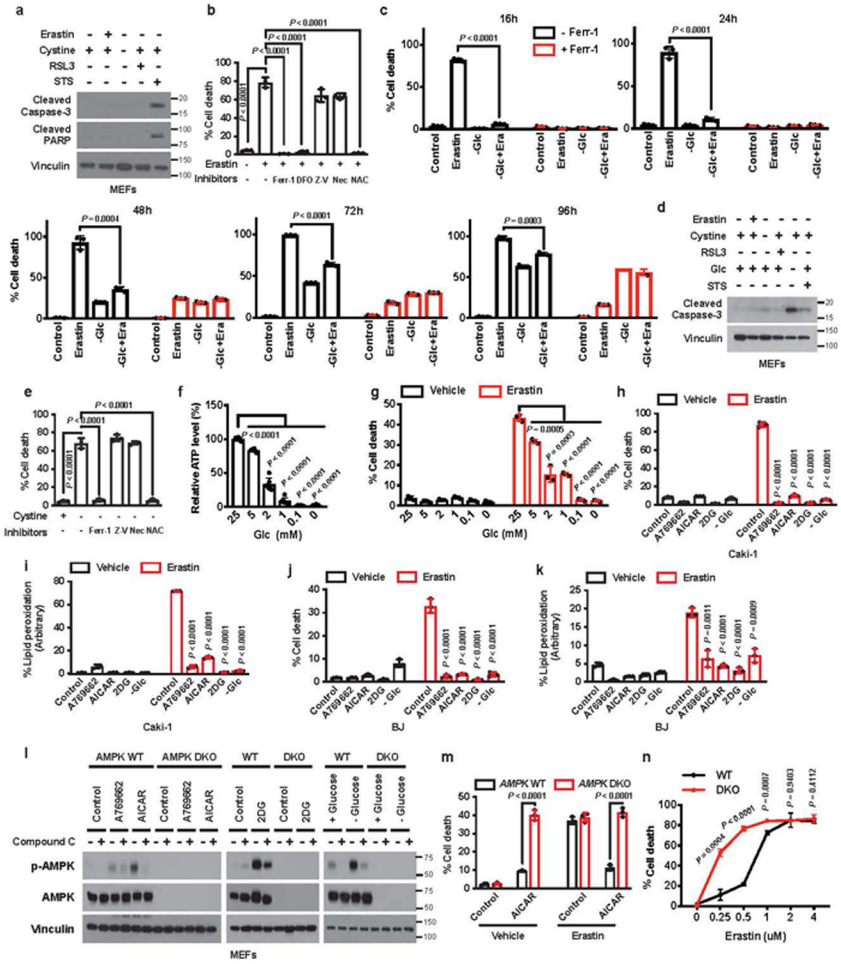

Extended Data Fig. 1. Energy stress inhibits ferroptosis

a, Immunoblot analysis in MEFs treated with 2 μM erastin (16 h), cysteine free media (8 h), 100 nM RSL3 (16 h), or 1 μM of staurosporine (STS, 2 h). **b**, Cell death measurement in MEFs treated with 2 μM erastin and cell death inhibitors for 16 h. Ferr-1: 1 μM ferrostatin-1; DFO: 100 μM deferoxamine; Z-V: 20 μM Z-VAD-FMK; Nec: 2 μM necrostatin-1; NAC: 5 mM N-acetyl cysteine. **c**, Cell death measurement in MEFs cultured in 25 or 0 mM glucose-containing medium with erastin and/or Ferrostatin-1 for the indicated times. **d**, Immunoblot analysis in MEFs treated as in **a**, or glucose starvation for 48 h. **e**, Cell death measurement in MEFs cultured in cystine free media with cell death inhibitors for 8 h. **f**, **g**, Intracellular ATP levels (**f**) and cell death measurement (**g**) in MEFs cultured with the indicated concentrations of glucose for 16 h. **h-k,** The measurement of cell death (**h**, **j**) and lipid peroxidation (**i**, **k**) in Caki-1 or BJ cells. Cells were treated with A769662 (200 μM), AICAR (2 mM), 2DG (5 mM), 0 mM glucose with simultaneous treatment of 2 μM erastin for 24 h (cell death) and 16 h (Lipid peroxidation). *P* values correspond to the comparison between control and each treatment in red bars. **l**, Immunoblot showing the levels of AMPK T172 phosphorylation. MEFs cells were treated as in **h-k** and compound C (5 μM) for 16 h. **m**, Cell death measurement in *AMPK* WT and DKO MEFs treated with 2 μM erastin and 2 mM of AICAR for 16 h. **n**, Cell death measurement in *AMPK* WT and DKO MEFs treated with erastin at

the indicated concentrations for 16 h. *P* values correspond to the comparison between *AMPK* WT and DKO at indicated erastin concentrations. Data show the mean ± s.d., n = 3 independent experiments. Statistical analysis was performed using unpaired, two-tailed t-test. Numerical source data are provided in Source Data Extended Data Fig. 1. Scanned images of unprocessed blots are shown in Source Data Extended Data Fig. 1.

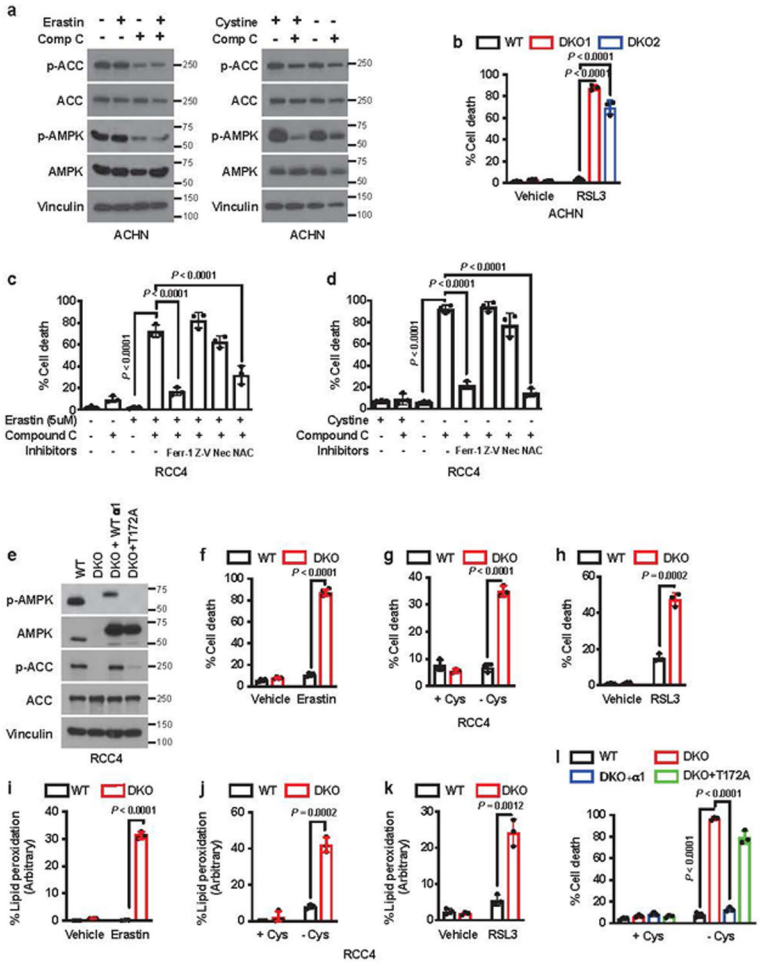

Extended Data Fig. 2. AMPK inactivation renders cells sensitive to ferroptotic cell death

a, Western blot showing the levels of ACC (S79) and AMPK (T172) phosphorylation in ACHN cells treated with erastin for 24 h or cultured in cystine-free media for 36 h with and without compound C (10 μM). **b,** Cell death measurement in *AMPK* WT and DKO ACHN cell lines treated with 100 nM RSL3 for 16 h. **c, d,** Cell death measurement in RCC4 cells treated with 10 μM of compound C, cell death inhibitors, and 5 μM of erastin for 24 h (**c**) or in cystine free media for 36 h (**d**). Ferr-1: 1 μM ferrostatin-1; Z-V: 20 μM Z-VAD-FMK; Nec: 2 μM necrostatin-1; NAC: 5 mM N-acetyl cysteine. **e**, Western blot showing the AMPK expression in RCC4 cell as indicated. **f-h**, Cell death measurement in *AMPK* WT and DKO RCC4 cell lines treated with 5 μM of erastin for 24 h (**f**), cultured in cystine free media for 24 h (**g**), or treated with 100 nM of RSL3 for 24 h (**h**). **i-k**, Lipid peroxidation measurement in *AMPK* WT and DKO RCC4 cells treated with 5 μM of erastin for 18 h (**i**), cultured in cystine free media for 18 h (**j**), or treated with 100 nM of RSL3 for 12 h (**k**). **l**, Cell death measurement in indicated RCC4 cells cultured with cystine free media for 24 h. Data show the mean ± s.d., n = 3 independent experiments. Statistical analysis was performed using unpaired, two-tailed t-test. Numerical source data are provided in Source Data Extended Data Fig. 2. Scanned images of unprocessed blots are shown in Source Data Extended Data Fig. 2.

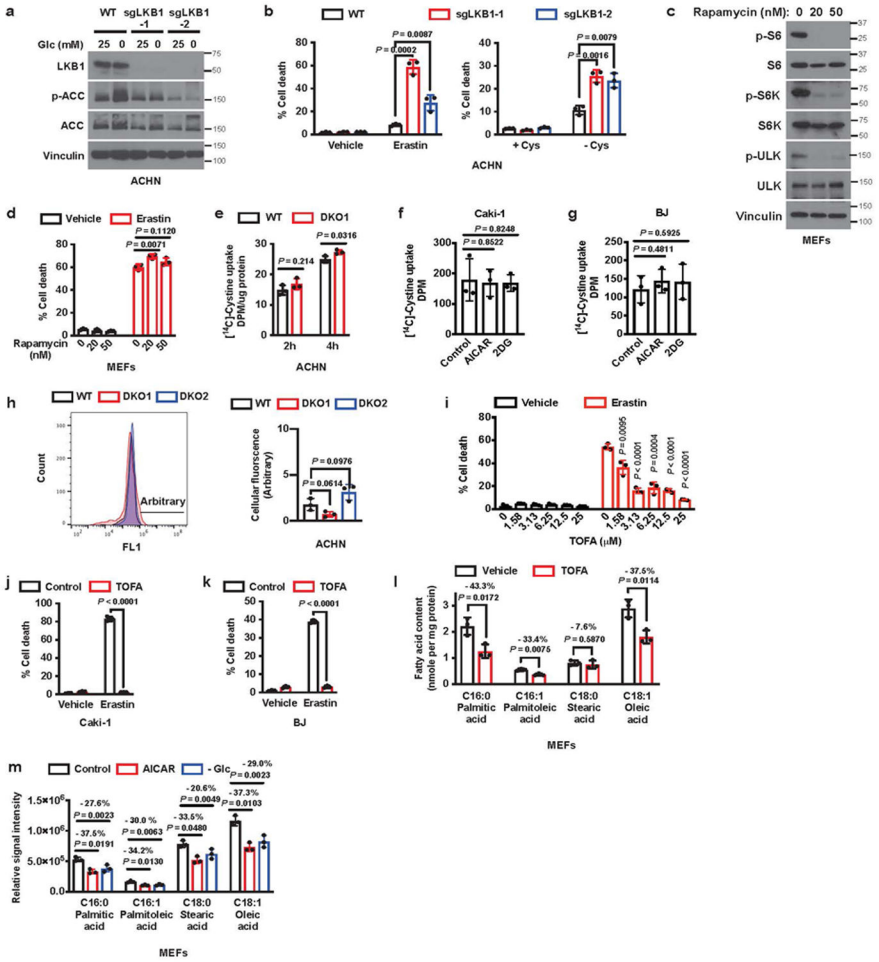

Extended Data Fig. 3. AMPK regulates ferroptosis partly through AMPK-mediated phosphorylation of ACC

a, Immunoblot blot indicating the loss of LKB1 in *LKB1* KO ACHN cells generated using CRISPR/CAS9 system. **b**, Cell death in *LKB1* WT and KO ACHN cells treated with 2 μM of erastin for 24 h and cultured in cystine free media for 24 h. **c**, Immunoblot blot showing mTOR inhibition in MEFs treated with rapamycin for 8 h. **d**, Cell death in MEFs treated with 2 μM of erastin and rapamycin for 16 h. **e**, The measurement of L-[^{14}C] Cystine uptake in *AMPK* WT and DKO ACHN cells. **f**, **g**, The measurement of L-[^{14}C] Cystine uptake in Caki-1 (**f**) and BJ (**g**) cells treated with 2 mM AICAR and 5 mM 2DG for 6h. **h**, The histograms and bar graphs showing the levels of intracellular labile iron in *AMPK* WT and DKO ACHN cells. **i**, Cell death measurement in MEFs treated with different TOFA concentrations and 2 μM erastin. *P* values correspond to the comparison between 0 μM and different conentrations of TOFA under erastin treatment. **j**,**k**, Cell death measurement in Caki-1 (**j**) and BJ (**k**) cells treated with 2 μM erastin and 50 μM TOFA for 24 h. l, m, The intracellular levels of the indicated free fatty acids in MEFs treated with vehicle or 25 μM of TOFA for 8 h (**l**) and treated with vehicle, 2 mM AICAR, or 0 mM glucose for 8 h (**m**). Data show the mean ± s.d., n = 3 independent experiments. Statistical analysis was performed using unpaired, two-tailed t-test. Numerical source data are provided in Source Data

Extended Data Fig. 3. Scanned images of unprocessed blots are shown in Source Data Extended Data Fig. 3.

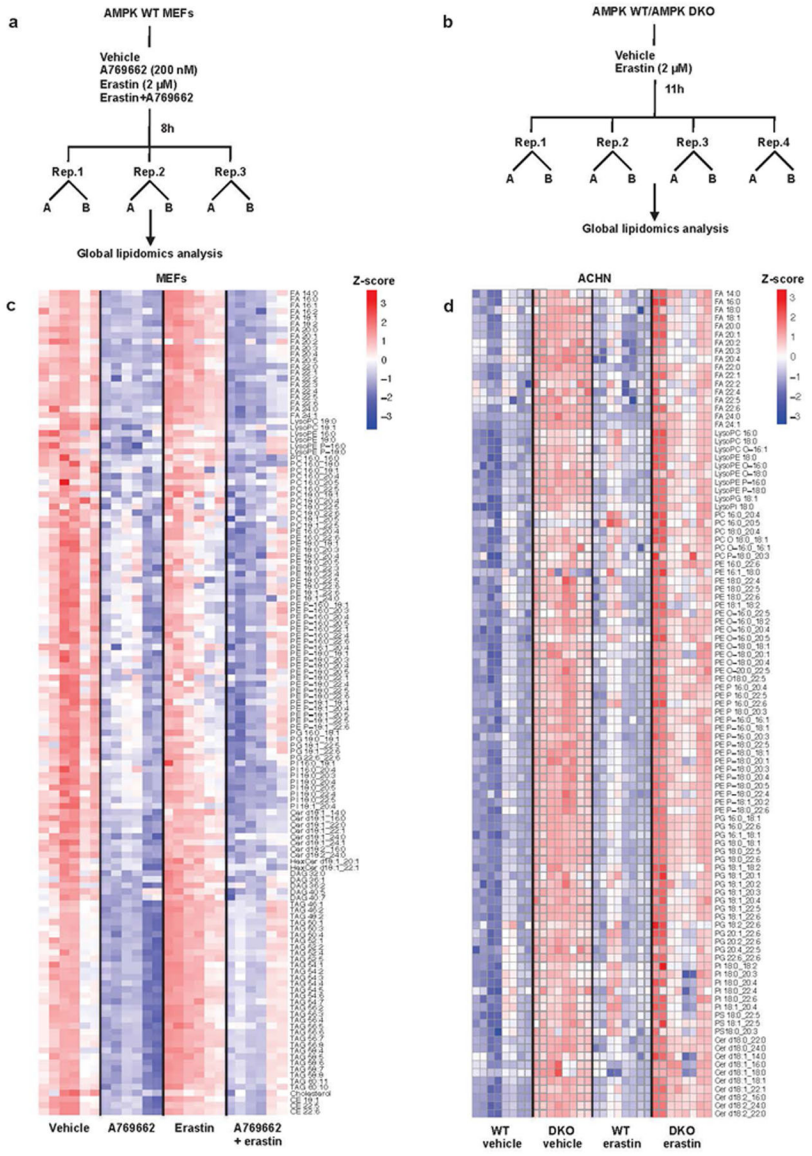

Extended Data Fig. 4. Lipidomic analyses upon AMPK activation or inactivation

a, **b**, Schematic diagram of the experimental design of mass spectrometry-based lipidomic analysis associated with AMPK activation. Global lipidomic analysis was performed in MEFs treated with vehicle, 2 μM erastin, 200 μM A769662, or 2 μM erastin + 200 μM A769662 for 8 h (**a**) or in *AMPK* WT and DKO ACHN cells treated with vehicle or 2 μM erastin for 11 h (**b**). There are three biologically independent samples (Rep. 1–3) in each group (**a**) and four biologically independent samples (Rep. 1–4) in each group (**b**). Samples ran in duplicates (two technical replicates: A, B) on the UPLC-MS. **c**, **d**, Heat map of significantly changed lipid species (One-way ANOVA, FDR corrected p-value < 0.05) in MEFs treated with vehicle, 2 μM erastin, 200 μM A769662, or 2 μM erastin + 200 μM A769662 (**c**) or in *AMPK* WT and DKO ACHN cells treated with vehicle or 2 μM erastin (**d**) combined in both positive and negative ionization modes. Each row represents z-score-normalized intensities of the detected lipid species. Each column represents a sample. The

relative abundance of each lipid is color-coded with red indicating high signal intensity and blue indicating low signal intensity. (FA, free fatty acid; Cer, ceramide; PC, phosphatidylcholine; LysoPC, lysophosphatidylcholine; PC O, ether-linked PC; PC P, plasmalogen PC; LysoPC O, ether-linked LysoPC; PE, phosphatidylethanolamine; LysoPE, lysophosphatidylethanolamine; PE O, ether-linked PE; PE P, plasmalogen PE; LysoPE O, ether-linked LysoPE; LysoPE P, plasmalogen LysoPE P; PG, phosphatidylglycerol; LysoPG, lyso phosphatidylglycerol; PI, phosphatidylinositol; LysoPI, lyso phosphatidylinositol; PA, phosphatidic acid; PS, phosphatidylserine; TAG, triacylglycerol; CE, cholesteryl ester. Lipids are annotated based on the fatty acyl compositions (e.g. LysoPC 16:0, 16 carbons and 0 double bond) or as sum of total number of carbons and double bonds (e.g. TAG 52:5, total of 52 carbons and 5 double bonds).

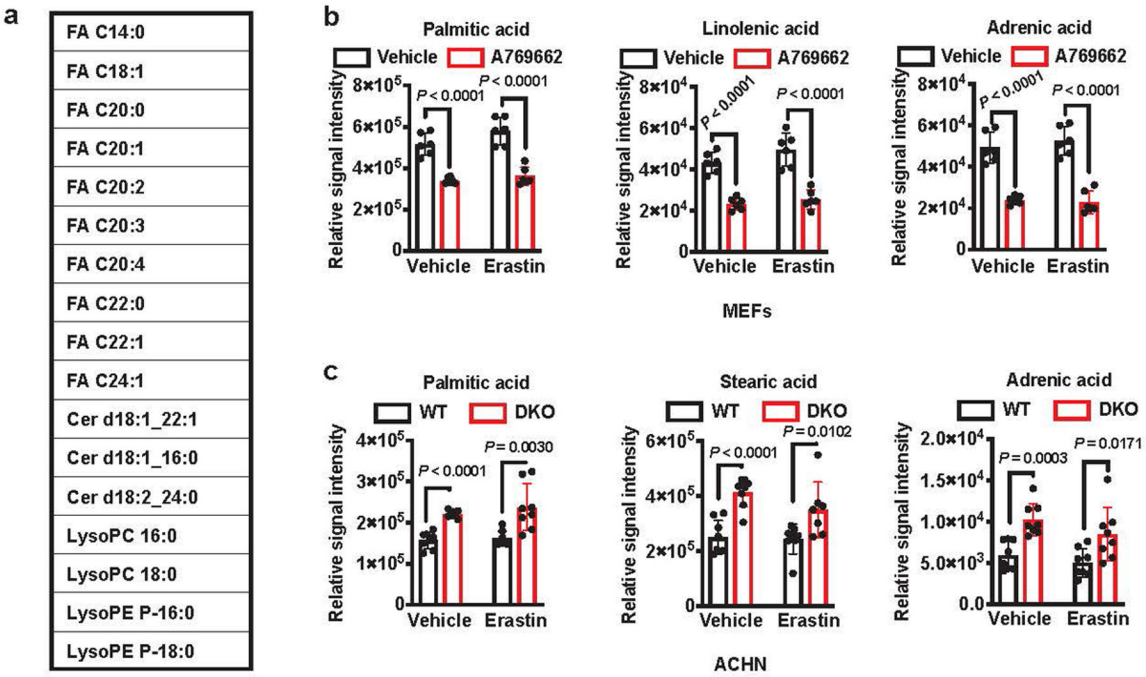

Extended Data Fig. 5. The levels of fatty acids were altered by AMPK activation or inactivation

a, List of 17 lipid species significantly changed (Two-tailed, unpaired Welch's t-test, Fold change ≥ 1.5 and FDR-corrected *p*-value < 0.05) in both MEFs (vehicle versus A769662) and ACHN (*AMPK* WT versus DKO) cells. Refer to Extended Data Fig. 4 for detailed sample information. **b**, **c**, The relative signal intensities of the indicated free fatty acids involved in long chain fatty acid biosynthesis in MEFs (**b**) or ACHN (**c**) cells with the indicated treatment and genotypes. Data show the mean ± s.d., n = 6 (**b**) or n = 8 (**c**) independent experiments. Statistical analysis was performed using unpaired, two-tailed t-test. Numerical source data are provided in Source Data Extended Data Fig. 5.

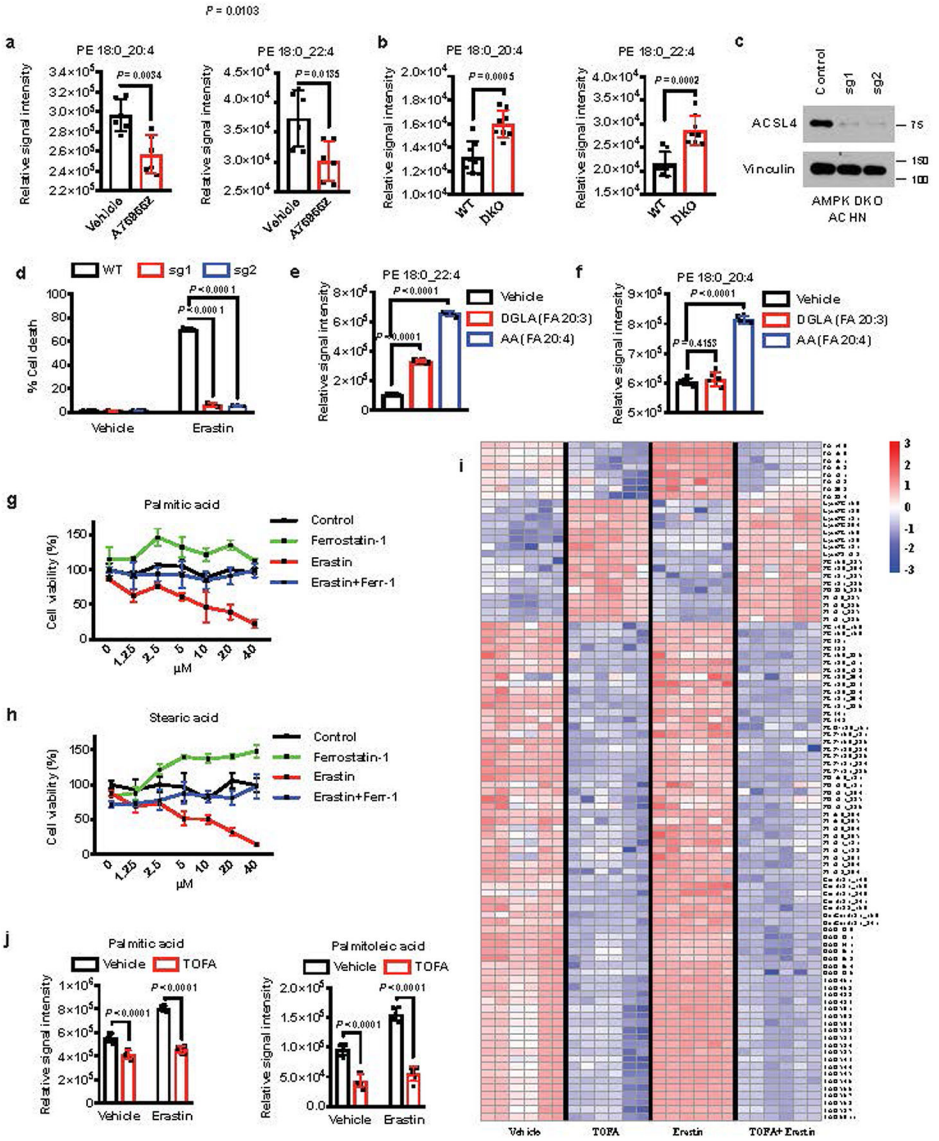

Extended Data Fig. 6. AMPK activation suppresses PUFA biosynthesis

a, **b**, The relative signal intensities of PE 18:0_20:4 and PE 18:0_22:4 in MEFs treated with A769662 (**a**) or *AMPK* WT and DKO ACHN cells (**b**). **c**, Immunoblot indicating the loss of ACSL4 in *AMPK* DKO ACHN cells. The experiment was repeated twice, independently, with similar results. **d**, Cell death in *AMPK* DKO ACHN cells with *ACSL4* WT and KO upon treatment of 2 μM erastin. **e**, **f**, The relative signal intensities of PE 18:0_22:4 (**e**) and PE 18:0_20:4 (**f**) in ACHN cells treated with 20 μM dihomo-γ-linolenic acid or arachidonic acid for 42 h. **g**, **h**, Cell viability measurement in ACHN cells incubated with palmitic acid (**g**) or stearic acid (**h**) with a series of concentration (0 μM-40 μM) and treated with or without ferrostatin-1 (Ferr-1) or erastin as indicated. **i**, Heat map of significantly changed lipid species (One-way ANOVA, FDR corrected *p*-value < 0.05) in MEFs treated with vehicle, 25 μM TOFA, 2 μM erastin, or 25μM TOFA+2 μM erastin combined positive and negative ionization modes. There are three biologically independent samples in each group and the samples analyzed in duplicates (technical replicates) on the UPLC-MS. Each row

represents z-score-normalized relative signal intensities of the identified lipid species. Each column represents a sample. The relative abundance of each lipid is color-coded with red indicating high signal intensity and blue indicating low signal intensity. **j**, The relative signal intensities of the indicated fatty acids in MEFs treated with vehicle or 25 μM TOFA. Data show the mean ± s.d., n = 3 (**d**, **g**, **h**), n = 6 (**a**, **e**, **f**, **j**) or n = 8 (**b**) independent experiments. Statistical analysis was performed using unpaired, two-tailed t-test. Scanned images of unprocessed blots are shown in Source Data Extended Data Fig. 6. Numerical source data are provided in Source Data Extended Data Fig. 6.

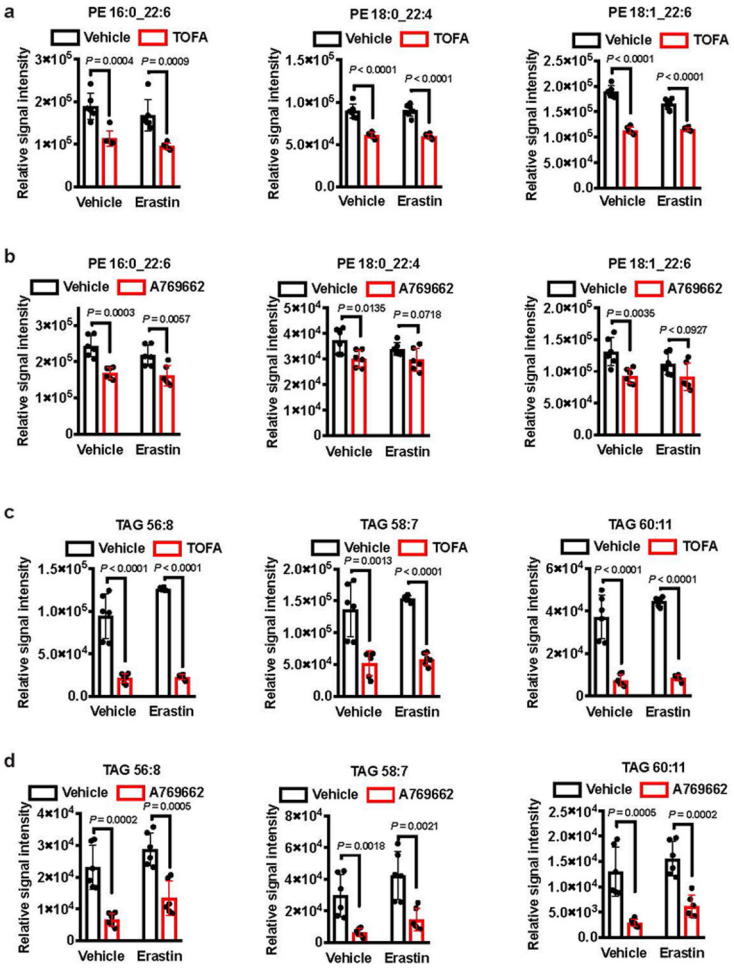

Extended Data Fig. 7. Lipidomics analysis in MEFs treated with A769662 or TOFA

a, **b**, The relative signal intensities of the same PUFA-containing PEs in MEFs treated with 25 μM TOFA (**a**) or 200 μM A769662 (**b**). **c**, **d**, The relative signal intensities of TAGs with the same number of carbons and double bonds in MEFs treated with 25 μM TOFA (**c**) or 200 μM A769662 (**d**). Data show the mean ± s.d., n = 6 independent experiments. Statistical analysis was performed using unpaired, two-tailed t-test. Numerical source data are provided in Source Data Extended Data Fig. 7.

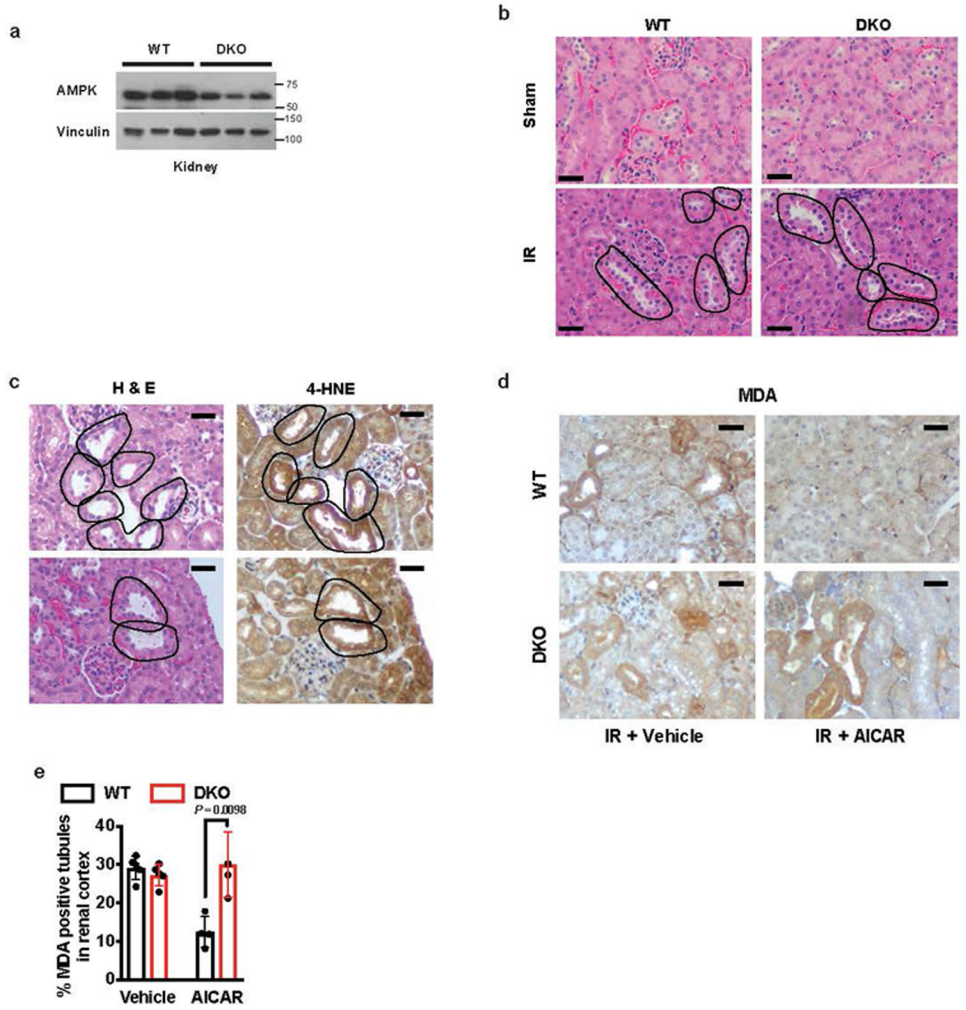

Extended Data Fig. 8. Renal ischemia reperfusion injury in in *AMPK* α1/α2$^{L/L}$ or *AMPKα1/α2*$^{L/L}$, *Rosa26-CreERT2* mice

a, Immunoblot showing the levels of AMPK α expression in kidneys of three individual *AMPK* α1/α2$^{L/L}$ or *AMPKα1/α2*$^{L/L}$, *Rosa26-CreERT2* mice (referred to as *AMPK* WT and KO mice). The experiment was repeated three times, independently, with similar results. **b**, Representative images of hematoxylin and eosin (H&E) staining of the renal cortex in sham-treated and IR-operated *AMPK* WT or DKO mice. Damaged renal tubules are marked by black dotted lines. Scale bars, 50 μm. The experiment was repeated more than ten times, independently, with similar results. **c**, Representative images of H&E staining and immunohistochemical staining of 4-HNE from mouse renal cortex after IR. Damaged renal tubules are marked with black dotted lines and 4-HNE stained tubules are marked with red dotted lines. Scale bars, 50 μm. The experiment was repeated more than ten times, independently, with similar results. **d**, **e**, Representative images showing MDA immunohistochemical staining from mouse renal cortex with the indicated genotypes and treatment conditions (**d**; dark brown stained tubules indicate MDA positive staining, Scale bars, 50 μm). Bar graphs presenting the percentages of MDA positive tubules per visual field (**e**). Data show the mean ± s.d., n = 4 (AICAR) or n = 5 (vehicle) independent experiments. Statistical analysis was performed using unpaired, two-tailed t-test. Scanned images of

unprocessed blots are shown in Source Data Extended Data Fig. 8. Numerical source data are provided in Source Data Extended Data Fig. 8.

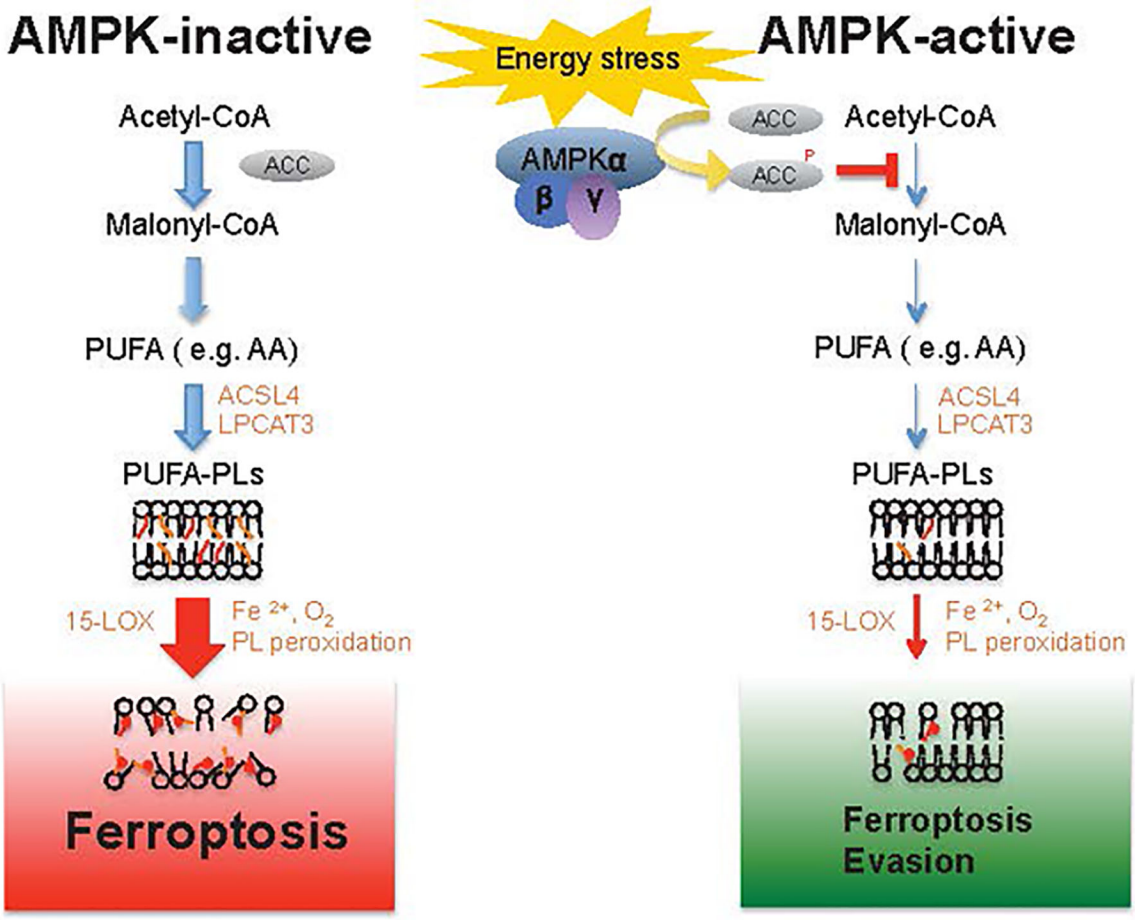

Extended Data Fig. 9. A schematic model describing the roles of AMPK-mediated energy stress signaling in regulating ferroptosis

See discussion for the detailed description. ACC: acetyl-CoA carboxylase; PUFAs: polyunsaturated fatty acids; AA: arachidonic acid; PUFA-PLs: polyunsaturated fatty acid-containing phospholipids; ACSL4: acyl-CoA synthetase long chain family member 4; LPCAT3: lysophosphatidylcholine acyltransferase 3; 15-LOX: 15-lipoxygenase.

Supplementary Material

Refer to Web version on PubMed Central for supplementary material.

Acknowledgements

We thank Lewis Brown for providing access to instrumentation for lipidomics experiments. This research has been supported by the Andrew Sabin Family Fellow Award, and Bridge Fund from The University of Texas MD Anderson Cancer Center (to B.G.), and grants from the National Institutes of Health (R01CA181196 to B.G.; R35CA209896, 1R61NS109407 and P01CA087497 to B.R.S.; R01CA166051 and R01CA181029 to L.M.). J.K.M. is supported by Susan G. Komen PDF Basic/Translational and Clinical Funding Program (PDF17487931). T.F.W. is supported in part by the DOD (1W81XWH-18-1-0573), the NIH and NCI (1R01CA215226), The Welch Foundation (Q-0007), and the McNair Medical Institute. G.R.S. is supported by a Canada Research Chair and the J. Bruce Duncan Chair in Metabolic Diseases and research grants from the Canadian Institutes of Health Research (201709FDN-CEBA-116200) and Diabetes Canada (DI-5-17-5302-GS). B.G. is an Andrew Sabin Family Fellow. This research has also been supported by the National Institutes of Health Cancer Center Support Grant P30CA016672 to The University of Texas MD Anderson Cancer Center.

References

1. Green DR, Galluzzi L & Kroemer G Cell biology. Metabolic control of cell death. Science 345, 1250256 (2014). [PubMed: 25237106]
2. Hardie DG, Ross FA & Hawley SA AMPK: a nutrient and energy sensor that maintains energy homeostasis. Nat Rev Mol Cell Biol 13, 251–262 (2012). [PubMed: 22436748]
3. Hardie DG, Schaffer BE & Brunet A AMPK: An Energy-Sensing Pathway with Multiple Inputs and Outputs. Trends in cell biology (2015).
4. El Mjiyad N, Caro-Maldonado A, Ramirez-Peinado S & Munoz-Pinedo C Sugar-free approaches to cancer cell killing. Oncogene 30, 253–264 (2011). [PubMed: 20972457]
5. Lin A et al. The FoxO-BNIP3 axis exerts a unique regulation of mTORC1 and cell survival under energy stress. Oncogene 33, 3183–3194 (2014). [PubMed: 23851496]
6. Dixon SJ et al. Ferroptosis: an iron-dependent form of nonapoptotic cell death. Cell 149, 1060–1072 (2012). [PubMed: 22632970]
7. Xie Y et al. Ferroptosis: process and function. Cell Death Differ 23, 369–379 (2016). [PubMed: 26794443]
8. Cao JY & Dixon SJ Mechanisms of ferroptosis. Cell Mol Life Sci 73, 2195–2209 (2016). [PubMed: 27048822]
9. Yang WS & Stockwell BR Ferroptosis: Death by Lipid Peroxidation. Trends in cell biology 26, 165–176 (2016). [PubMed: 26653790]
10. Stockwell BR et al. Ferroptosis: A Regulated Cell Death Nexus Linking Metabolism, Redox Biology, and Disease. Cell 171, 273–285 (2017). [PubMed: 28985560]
11. Jiang L et al. Ferroptosis as a p53-mediated activity during tumour suppression. Nature 520, 57–62 (2015). [PubMed: 25799988]
12. Gao M, Monian P, Quadri N, Ramasamy R & Jiang X Glutaminolysis and Transferrin Regulate Ferroptosis. Mol Cell 59, 298–308 (2015). [PubMed: 26166707]
13. Linkermann A et al. Synchronized renal tubular cell death involves ferroptosis. Proc Natl Acad Sci U S A 111, 16836–16841 (2014). [PubMed: 25385600]
14. Zhang Y et al. BAP1 links metabolic regulation of ferroptosis to tumour suppression. Nat Cell Biol 20, 1181–1192 (2018). [PubMed: 30202049]
15. Chen L, Hambright WS, Na R & Ran Q Ablation of the Ferroptosis Inhibitor Glutathione Peroxidase 4 in Neurons Results in Rapid Motor Neuron Degeneration and Paralysis. J Biol Chem 290, 28097–28106 (2015). [PubMed: 26400084]
16. Do Van B et al. Ferroptosis, a newly characterized form of cell death in Parkinson's disease that is regulated by PKC. Neurobiol Dis 94, 169–178 (2016). [PubMed: 27189756]
17. Shimada K et al. Global survey of cell death mechanisms reveals metabolic regulation of ferroptosis. Nature chemical biology 12, 497–503 (2016). [PubMed: 27159577]
18. Yang WS et al. Regulation of ferroptotic cancer cell death by GPX4. Cell 156, 317–331 (2014). [PubMed: 24439385]
19. Friedmann Angeli JP et al. Inactivation of the ferroptosis regulator Gpx4 triggers acute renal failure in mice. Nat Cell Biol 16, 1180–1191 (2014). [PubMed: 25402683]
20. Koppula P, Zhang Y, Zhuang L & Gan B Amino acid transporter SLC7A11/xCT at the crossroads of regulating redox homeostasis and nutrient dependency of cancer. Cancer Commun (Lond) 38, 12 (2018). [PubMed: 29764521]
21. Dai F et al. BAP1 inhibits the ER stress gene regulatory network and modulates metabolic stress response. Proc Natl Acad Sci U S A 114, 3192–3197 (2017). [PubMed: 28275095]
22. Hay N Reprogramming glucose metabolism in cancer: can it be exploited for cancer therapy? Nat Rev Cancer 16, 635–649 (2016). [PubMed: 27634447]
23. Inoki K, Zhu T & Guan KL TSC2 mediates cellular energy response to control cell growth and survival. Cell 115, 577–590 (2003). [PubMed: 14651849]
24. Shaw RJ et al. The tumor suppressor LKB1 kinase directly activates AMP-activated kinase and regulates apoptosis in response to energy stress. Proc Natl Acad Sci U S A 101, 3329–3335 (2004). [PubMed: 14985505]

25. Liu X et al. LncRNA NBR2 engages a metabolic checkpoint by regulating AMPK under energy stress. Nat Cell Biol 18, 431–442 (2016). [PubMed: 26999735]
26. Hou W et al. Autophagy promotes ferroptosis by degradation of ferritin. Autophagy 12, 1425–1428 (2016). [PubMed: 27245739]
27. Gao M et al. Ferroptosis is an autophagic cell death process. Cell research 26, 1021–1032 (2016). [PubMed: 27514700]
28. Bianchi A, Evans JL, Nordlund AC, Watts TD & Witters LA Acetyl-CoA carboxylase in Reuber hepatoma cells: variation in enzyme activity, insulin regulation, and cellular lipid content. Journal of cellular biochemistry 48, 86–97 (1992). [PubMed: 1349893]
29. Houde VP et al. AMPK beta1 reduces tumor progression and improves survival in p53 null mice. Mol Oncol 11, 1143–1155 (2017). [PubMed: 28544264]
30. Fullerton MD et al. Single phosphorylation sites in Acc1 and Acc2 regulate lipid homeostasis and the insulin-sensitizing effects of metformin. Nat Med 19, 1649–1654 (2013). [PubMed: 24185692]
31. Yang WS et al. Peroxidation of polyunsaturated fatty acids by lipoxygenases drives ferroptosis. Proc Natl Acad Sci U S A 113, E4966–4975 (2016). [PubMed: 27506793]
32. Skouta R et al. Ferrostatins inhibit oxidative lipid damage and cell death in diverse disease models. J Am Chem Soc 136, 4551–4556 (2014). [PubMed: 24592866]
33. Kagan VE et al. Oxidized arachidonic and adrenic PEs navigate cells to ferroptosis. Nature chemical biology 13, 81–90 (2017). [PubMed: 27842066]
34. Doll S et al. ACSL4 dictates ferroptosis sensitivity by shaping cellular lipid composition. Nature chemical biology 13, 91–98 (2017). [PubMed: 27842070]
35. Chhipa RR et al. AMP kinase promotes glioblastoma bioenergetics and tumour growth. Nat Cell Biol 20, 823–835 (2018). [PubMed: 29915361]
36. Wang LT et al. Protective role of AMP-activated protein kinase-evoked autophagy on an in vitro model of ischemia/reperfusion-induced renal tubular cell injury. PLoS One 8, e79814 (2013). [PubMed: 24223196]
37. Decleves AE, Sharma K & Satriano J Beneficial Effects of AMP-Activated Protein Kinase Agonists in Kidney Ischemia-Reperfusion: Autophagy and Cellular Stress Markers. Nephron Exp Nephrol (2014).
38. Boroughs LK & DeBerardinis RJ Metabolic pathways promoting cancer cell survival and growth. Nat Cell Biol 17, 351–359 (2015). [PubMed: 25774832]
39. Gao M et al. Role of Mitochondria in Ferroptosis. Mol Cell 73, 354–363 e353 (2019). [PubMed: 30581146]
40. Herzig S & Shaw RJ AMPK: guardian of metabolism and mitochondrial homeostasis. Nat Rev Mol Cell Biol 19, 121–135 (2018). [PubMed: 28974774]
41. Song X et al. AMPK-Mediated BECN1 Phosphorylation Promotes Ferroptosis by Directly Blocking System Xc(−) Activity. Curr Biol 28, 2388–2399 e2385 (2018). [PubMed: 30057310]
42. Zhang Y, Zhuang L & Gan B BAP1 suppresses tumor development by inducing ferroptosis upon SLC7A11 repression. Molecular & cellular oncology 6, 1536845 (2019). [PubMed: 30788415]
43. Liu T, Jiang L, Tavana O & Gu W The Deubiquitylase OTUB1 Mediates Ferroptosis via Stabilization of SLC7A11. Cancer Res 79, 1913–1924 (2019). [PubMed: 30709928]
44. Chu B et al. ALOX12 is required for p53-mediated tumour suppression through a distinct ferroptosis pathway. Nat Cell Biol (2019).
45. Gan B DUBbing Ferroptosis in Cancer Cells. Cancer Res 79, 1749–1750 (2019). [PubMed: 30987975]
46. Hardie DG Molecular Pathways: Is AMPK a Friend or a Foe in Cancer? Clin Cancer Res 21, 3836–3840 (2015). [PubMed: 26152739]
47. Shackelford DB & Shaw RJ The LKB1-AMPK pathway: metabolism and growth control in tumour suppression. Nat Rev Cancer 9, 563–575 (2009). [PubMed: 19629071]
48. Saito Y, Chapple RH, Lin A, Kitano A & Nakada D AMPK Protects Leukemia-Initiating Cells in Myeloid Leukemias from Metabolic Stress in the Bone Marrow. Cell Stem Cell 17, 585–596 (2015). [PubMed: 26440282]

49. Kishton RJ et al. AMPK Is Essential to Balance Glycolysis and Mitochondrial Metabolism to Control T-ALL Cell Stress and Survival. Cell Metab 23, 649–662 (2016). [PubMed: 27076078]
50. Eichner LJ et al. Genetic Analysis Reveals AMPK Is Required to Support Tumor Growth in Murine Kras-Dependent Lung Cancer Models. Cell Metab (2018).
51. Jeon SM, Chandel NS & Hay N AMPK regulates NADPH homeostasis to promote tumour cell survival during energy stress. Nature 485, 661–665 (2012). [PubMed: 22660331]
52. Ross FA, MacKintosh C & Hardie DG AMP-activated protein kinase: a cellular energy sensor that comes in 12 flavours. FEBS J 283, 2987–3001 (2016). [PubMed: 26934201]
53. Gan B et al. mTORC1-dependent and -independent regulation of stem cell renewal, differentiation, and mobilization. Proc Natl Acad Sci U S A 105, 19384–19389 (2008). [PubMed: 19052232]
54. Gan B et al. FoxOs enforce a progression checkpoint to constrain mTORC1-activated renal tumorigenesis. Cancer Cell 18, 472–484 (2010). [PubMed: 21075312]
55. Lee H et al. BAF180 regulates cellular senescence and hematopoietic stem cell homeostasis through p21. Oncotarget 7, 19134–19146 (2016). [PubMed: 26992241]
56. Chauhan AS et al. STIM2 interacts with AMPK and regulates calcium-induced AMPK activation. FASEB J 33, 2957–2970 (2019). [PubMed: 30335546]
57. Xiao ZD et al. Energy stress-induced lncRNA FILNC1 represses c-Myc-mediated energy metabolism and inhibits renal tumor development. Nature communications 8, 783 (2017).
58. Liu X & Gan B lncRNA NBR2 modulates cancer cell sensitivity to phenformin through GLUT1. Cell Cycle 15, 3471–3481 (2016). [PubMed: 27792451]
59. Koppula P, Zhang Y, Shi J, Li W & Gan B The glutamate/cystine antiporter SLC7A11/xCT enhances cancer cell dependency on glucose by exporting glutamate. J Biol Chem 292, 14240–14249 (2017). [PubMed: 28630042]
60. Zhang Y, Koppula P & Gan B Regulation of H2A ubiquitination and SLC7A11 expression by BAP1 and PRC1. Cell Cycle, 1–11 (2019).
61. Gan B et al. Lkb1 regulates quiescence and metabolic homeostasis of haematopoietic stem cells. Nature 468, 701–704 (2010). [PubMed: 21124456]
62. Lin A et al. FoxO transcription factors promote AKT Ser473 phosphorylation and renal tumor growth in response to pharmacological inhibition of the PI3K-AKT pathway. Cancer Res (2014).
63. Gan B, Yoo Y & Guan JL Association of focal adhesion kinase with tuberous sclerosis complex 2 in the regulation of s6 kinase activation and cell growth. J Biol Chem 281, 37321–37329 (2006). [PubMed: 17043358]
64. Gan B, Melkoumian ZK, Wu X, Guan KL & Guan JL Identification of FIP200 interaction with the TSC1-TSC2 complex and its role in regulation of cell size control. J Cell Biol 170, 379–389 (2005). [PubMed: 16043512]
65. Matyash V, Liebisch G, Kurzchalia TV, Shevchenko A & Schwudke D Lipid extraction by methyl-tert-butyl ether for high-throughput lipidomics. Journal of lipid research 49, 1137–1146 (2008). [PubMed: 18281723]
66. Zhang Y et al. Imidazole Ketone Erastin Induces Ferroptosis and Slows Tumor Growth in a Mouse Lymphoma Model. Cell Chem Biol (2019).
67. Smith CA, Want EJ, O'Maille G, Abagyan R & Siuzdak G XCMS: processing mass spectrometry data for metabolite profiling using nonlinear peak alignment, matching, and identification. Anal Chem 78, 779–787 (2006). [PubMed: 16448051]
68. Tautenhahn R, Bottcher C & Neumann S Highly sensitive feature detection for high resolution LC/MS. BMC Bioinformatics 9, 504 (2008). [PubMed: 19040729]
69. Chong J et al. MetaboAnalyst 4.0: towards more transparent and integrative metabolomics analysis. Nucleic Acids Res 46, W486–W494 (2018). [PubMed: 29762782]

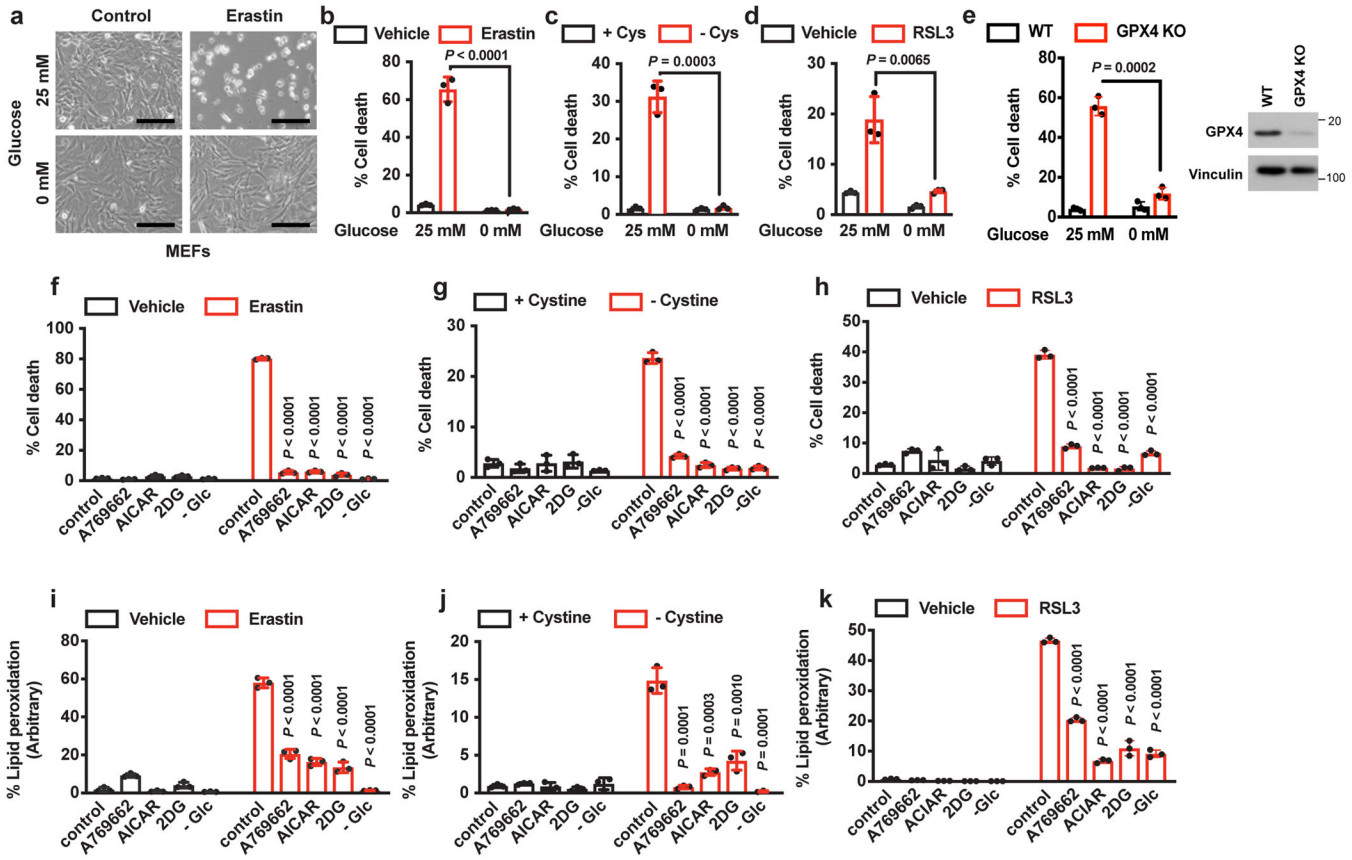

Fig. 1. Energy stress inhibits ferroptotic cell death.

a, Representative images showing the induction of cell death in immortalized MEFs treated with 2 μM erastin cultured in 25 mM or 0 mM glucose for 16 h. Scale bars, 100 μm. **b-d**, Cell death measurement in MEFs cultured in 25 mM or 0 mM glucose and treated with 2 μM erastin for 16 h (**b**), cultured in cysteine-free media for 8 h (**c**), or treated with 100 nM RLS3 for 16 h (**d**). **e**, Cell death measurement in *GPX4* WT and KO Caki-1 cells cultured in 25 or 0 mM glucose for 16 h and immunoblot showing the levels of GPX4. **f-h**, Cell death measurement in MEFs treated with energy stress inducer/mimetic agents including A769662 (200 μM), AICAR (2 mM), 2DG (5 mM), 0 mM glucose with simultaneous treatment of 2 μM erastin for 16 h (**f**), cystine-free media for 8 h (**g**), or 100 nM RSL3 for 16 h (**h**). *P* values correspond to the comparison between control and each treatment in red bars. **i-k**, Lipid peroxidation in MEFs treated with energy stress inducer/mimetic agents and 2 μM erastin for 8 h (**i**), cystine-free media for 6 h (**j**), or 100 nM RSL3 for 8 h (**k**). *P* values correspond to the comparison between control and each treatment in red bars. Data show the mean ± s.d., n = 3 independent experiments. Statistical analysis was performed using unpaired, two-tailed t-test. Numerical source data are provided in Source Data Fig. 1. Scanned images of unprocessed blots are shown in Source Data Fig. 1.

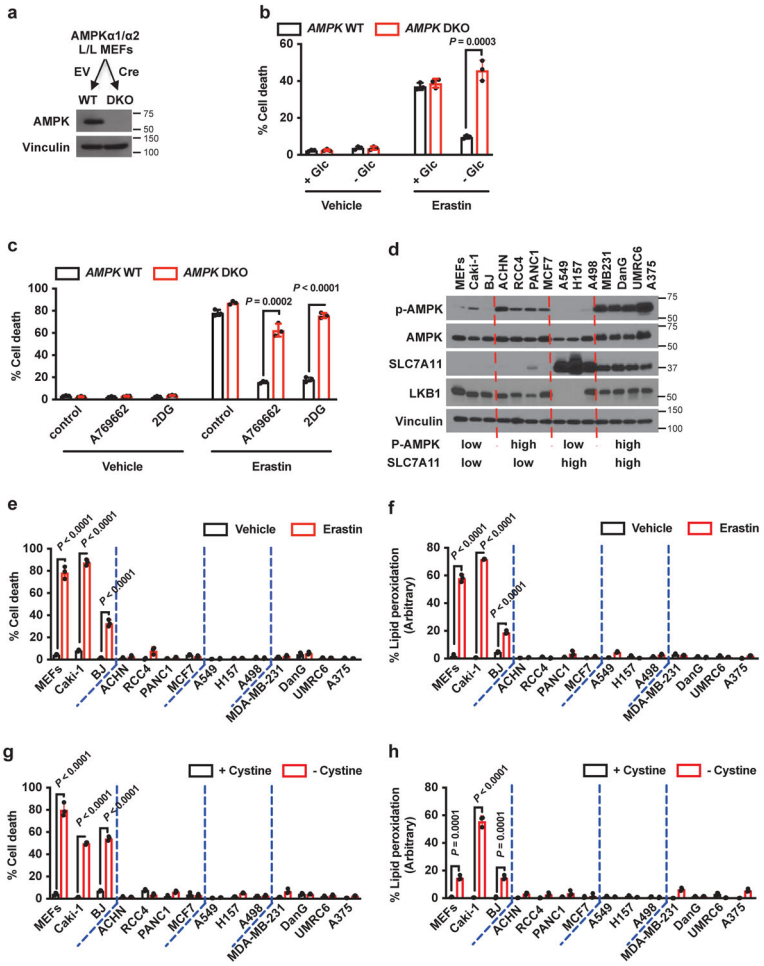

Fig. 2. Energy stress inhibits ferroptotic cell death partly through AMPK.

a, Immunoblot showing the levels of AMPKα in *AMPK* α1/α2 WT and DKO MEFs. **b**,**c**, Cell death measurement in *AMPK* WT and DKO MEFs treated with erastin (2 μM) cultured in 25 or 0 mM glucose for 16 h (**b**), or co-treated with A769662 (200 μM) or 2DG (5 mM) for 16 h (**c**). **d**, Immunoblot showing the levels of AMPK T172 phosphorylation, AMPK, SLC7A11 and LKB1 in cell lines as indicated. **e**, Cell death measurement in the indicated cell lines at 24 h after 2 μM erastin treatment. **f**, Lipid peroxidation measurement in the indicated cell lines treated with 2 μM of erastin for 24 h, except MEFs (8 h), Caki-1 (16 h), and BJ (16 h) cell lines. **g**, **h**, The measurement of cell death (**g**) and lipid peroxidation (**h**) in the indicated cell lines cultured in cystine free media for 36 h and 16 h, respectively. Lipid peroxidation in MEFs was measured at 6 h. Data show the mean ± s.d., n = 3 independent experiments. Statistical analysis was performed using unpaired, two-tailed t-test. Numerical source data are provided in Source Data Fig. 2. Scanned images of unprocessed blots are shown in Source Data Fig. 2.

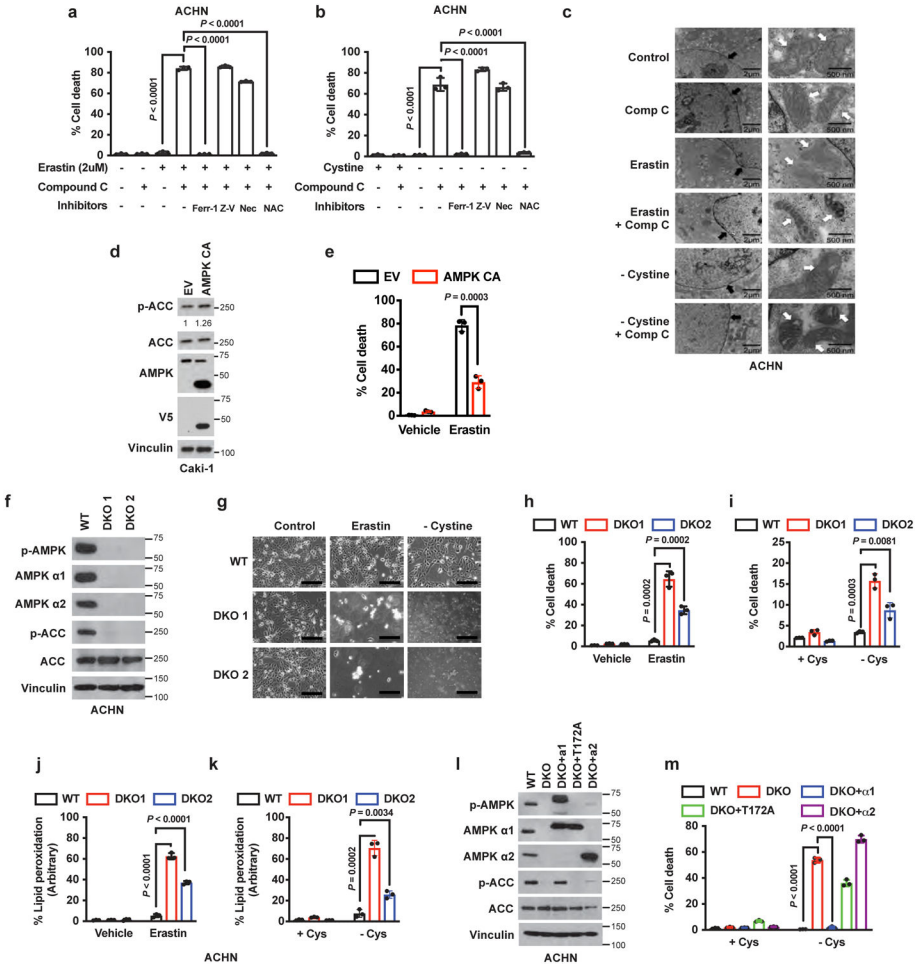

Fig. 3. AMPK inactivation sensitizes cells to ferroptotic cell death.

a,**b**, Cell death measurement in ACHN cells treated with AMPK inhibitor compound C, cell death inhibitors, and 2 μM erastin for 12 h (**a**) or in cysteine-free media for 36 h (**b**). Ferr-1: 1 μM ferrostatin-1; Z-V: 20 μM Z-VAD-FMK; Nec: 2 μM necrostatin-1s; NAC: 5 mM N-acetyl-cysteine. **c**, Transmission electron microscopy of ACHN cells with the indicated treatment for 9 h. Black arrows indicate nuclei; white arrows indicate mitochondria. Control: vehicle; Comp C: 10 μM Compound C; erastin: 2 μM erastin. Scale bars: left, 2 μm; right, 500 nm. **d**, Immunoblot showing the expression of AMPK CA in Caki-1 cells. **e**, Cell death measurement in Caki-1 cells expressing AMPK CA treated with 2 μM erastin for 16 h. **f**, Immunoblot indicating the loss of AMPK α1/α2 in *AMPK* DKO ACHN cell lines generated using CRISPR/Cas9 system. **g**, Representative phase-contrast images showing cell death induced by 2 μM erastin (24 h) or cystine withdrawal (36 h) in *AMPK* DKO ACHN cells. Scale bars, 100 μm. **h**, **I**, Cell death measurement in *AMPK* WT and DKO ACHN cells treated with 2 μM erastin for 18 h (**h**), or cultured in cystine-free media for 36 h (**i**). **j**, **k**, Lipid peroxidation measurement in *AMPK* WT and DKO ACHN cells treated with 2 μM erastin for 12 h (**j**), or cultured in cystine-free media for 18 h (**k**). **l**, Immunoblot showing the AMPK expression in ACHN cells as indicated. **m**, Measurement of cell death at 36 h post cystine withdrawal in ACHN cells as indicated. Data show the mean ± s.d., n = 3

independent experiments. Statistical analysis was performed using unpaired, two-tailed t-test. Numerical source data are provided in Source Data Fig. 3. Scanned images of unprocessed blots are shown in Source Data Fig. 3.

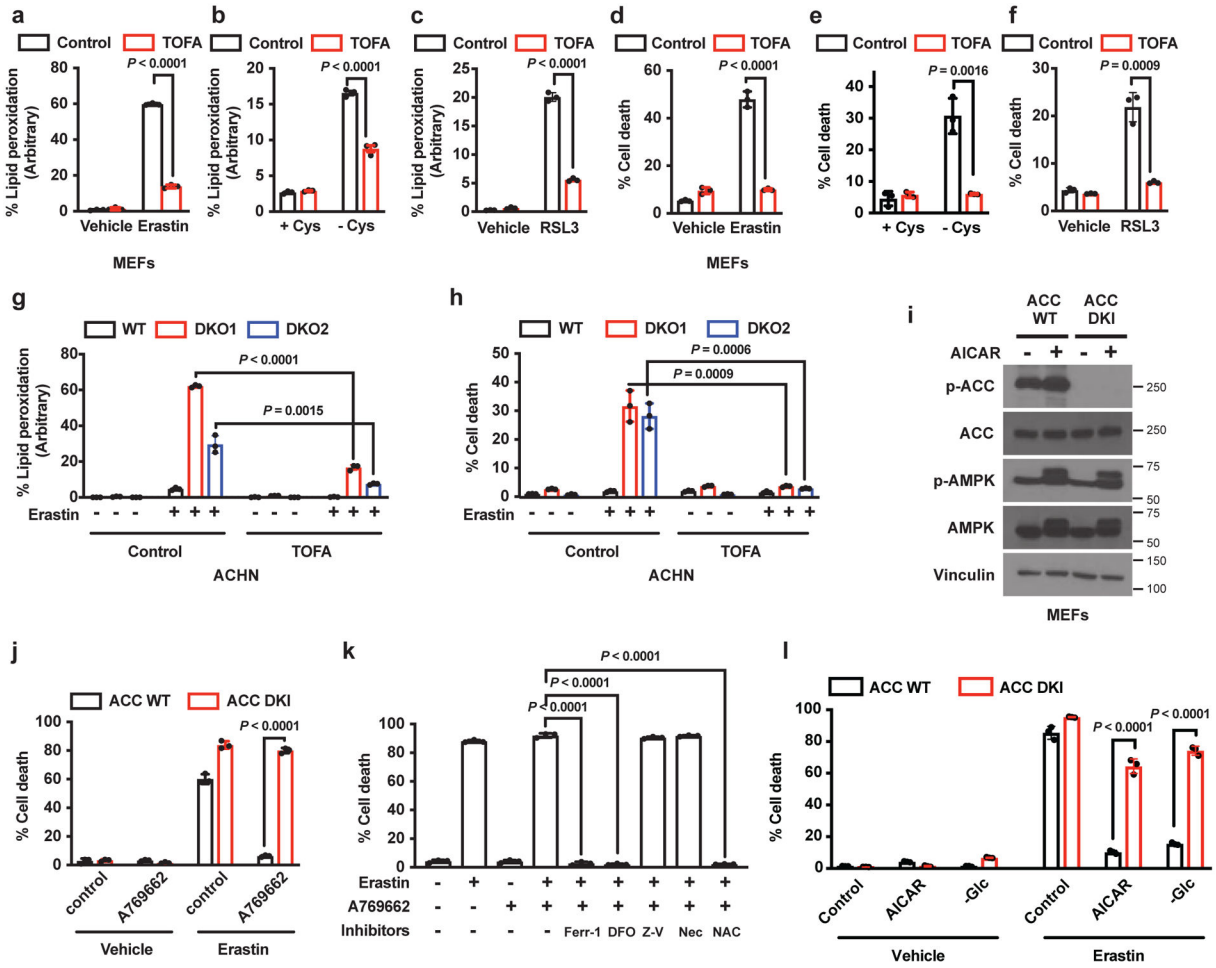

Fig. 4. AMPK-mediated phosphorylation of ACC inhibits ferroptosis.

a-c, Lipid peroxidation measurement in MEFs treated with or without 25 μM TOFA and 2 μM erastin for 8 h (**a**), cystine-free media for 6 h (**b**), or 100 nM RSL3 for 8 h (**c**). **d-f**, Cell death measurement in MEFs treated with or without 25 μM TOFA and 2 μM erastin for 16 h (**d**), cystine-free media for 8 h (**e**), or 100 nM RSL3 for 16 h (**f**). **g**, **h**, The measurement of lipid peroxidation (**g**) and cell death (**h**) in *AMPK* WT and DKO ACHN cells treated with 50 μM TOFA and 2 μM erastin for 12 h and 18 h, respectively. **I**, Immunoblot of *ACC* WT and *ACC1* (S79A)/*ACC2* (S212A) mutant double knock-in (DKI) immortalized MEFs. **j**, Cell death measurement in *ACC* WT and DKI MEFs treated with 2 μM erastin and 200 μM A769662 for 16 h. **k**, Cell death measurement in *ACC* DKI MEFs treated with erastin, A769662, and various cell death inhibitors or NAC. Fer: 1 μM ferrostatin-1; DFO: 100 μM deferoxamine; Z-V: 20 μM Z-VAD-FMK; Nec: 2 μM necrostatin-1s; NAC: 5 mM N-acetyl-cysteine. **l**, Cell death measurement in *ACC* WT and DKI MEFs treated with 2 μM erastin and 2 mM AICAR or 0 mM glucose for 36 h. Data show the mean ± s.d., n = 3 independent experiments. Statistical analysis was performed using unpaired, two-tailed t-test. Numerical source data are provided in Source Data Fig. 4. Scanned images of unprocessed blots are shown in Source Data Fig. 4.

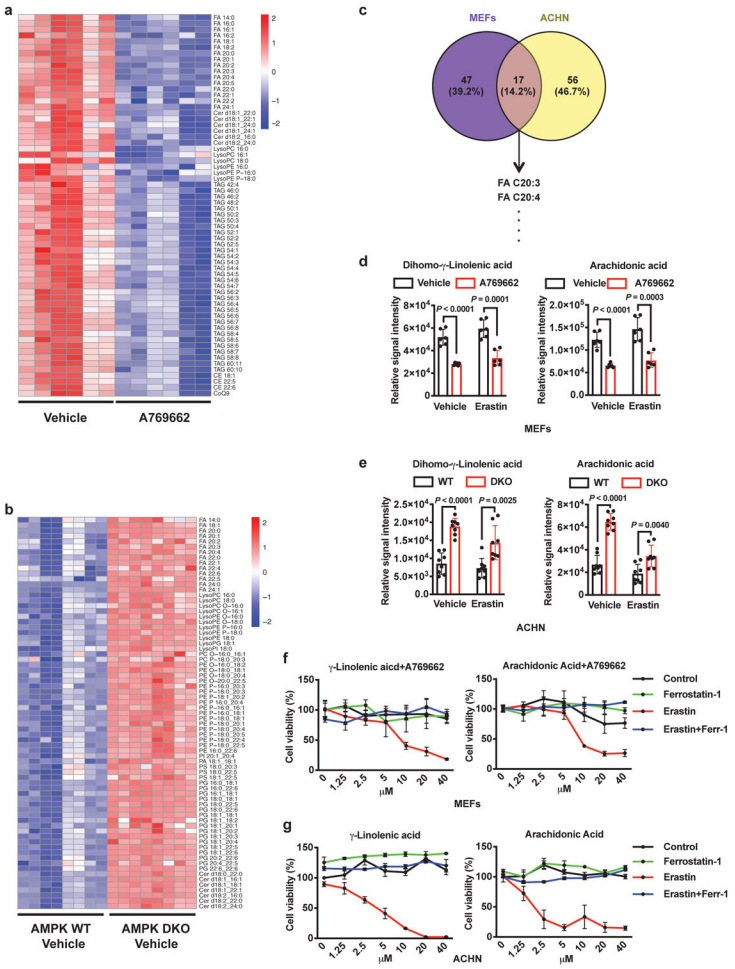

Fig. 5. AMPK regulates PUFA-containing lipid accumulation.

a, **b**, Heat maps of significantly changed lipid species (Two-tailed, unpaired Welch's t-test; fold change threshold = 1.5, FDR corrected *p*-value < 0.05; n =3 biologically independent samples) in vehicle- versus A769662-treated MEFs (**a**) and vehicle-treated *AMPK* WT versus DKO ACHN cells (**b**) measured in duplicates using UPLC-MS. Each row represents z-score-normalized intensities of the detected lipid species. Each column represents a sample. The relative abundance of each lipid is color-coded with red indicating high signal intensity and blue indicating low signal intensity (FA, free fatty acid; Cer, ceramide; PC, phosphatidylcholine; LysoPC, lysophosphatidylcholine; PC O, ether-linked PC; PC P, plasmalogen PC; LysoPC O, ether-linked LysoPC; PE, phosphatidylethanolamine; LysoPE, lysophosphatidylethanolamine; PE O, ether-linked PE; PE P, plasmalogen PE; LysoPE O, ether-linked LysoPE; LysoPE P, plasmalogen LysoPE P; PG, phosphatidylglycerol; LysoPG, lyso phosphatidylglycerol; PI, phosphatidylinositol; LysoPI, lyso phosphatidylinositol; PA, phosphatidic acid; PS, phosphatidylserine; TAG, triacylglycerol; CE, cholesteryl ester; CoQ9, coenzyme Q9). Lipids are annotated based on the fatty acyl compositions (e.g. LysoPC 16:0, 16 carbons and 0 double bond) or as sum of total number of carbons and double bonds (e.g. TAG 52:5, total of 52 carbons and 5 double bonds). **c**, Venn diagram depicting the numbers of significantly altered lipids from the comparison of MEFs and

ACHN cells. **d**, **e**, Relative signal intensities of dihomo-γ-linolenic acid and arachidonic acid in MEFs (**d**) and ACHN cells (**e**) with the indicated treatment and genotypes. **f**, **g**, Cell viability measurement in MEFs treated with A769662 (**f**) or ACHN WT cells (**g**) incubated with the indicated fatty acids with a series of concentrations (0 μM-40 μM) and treated with or without ferrostatin-1 (Ferr-1) or erastin as indicated. Data show the mean ± s.d., n = 3 (**f,g**), n = 6 (**d**) or n = 8 (**e**) independent experiments. Statistical analysis was performed using unpaired, two-tailed t-test. Numerical source data are provided in Source Data Fig. 5.

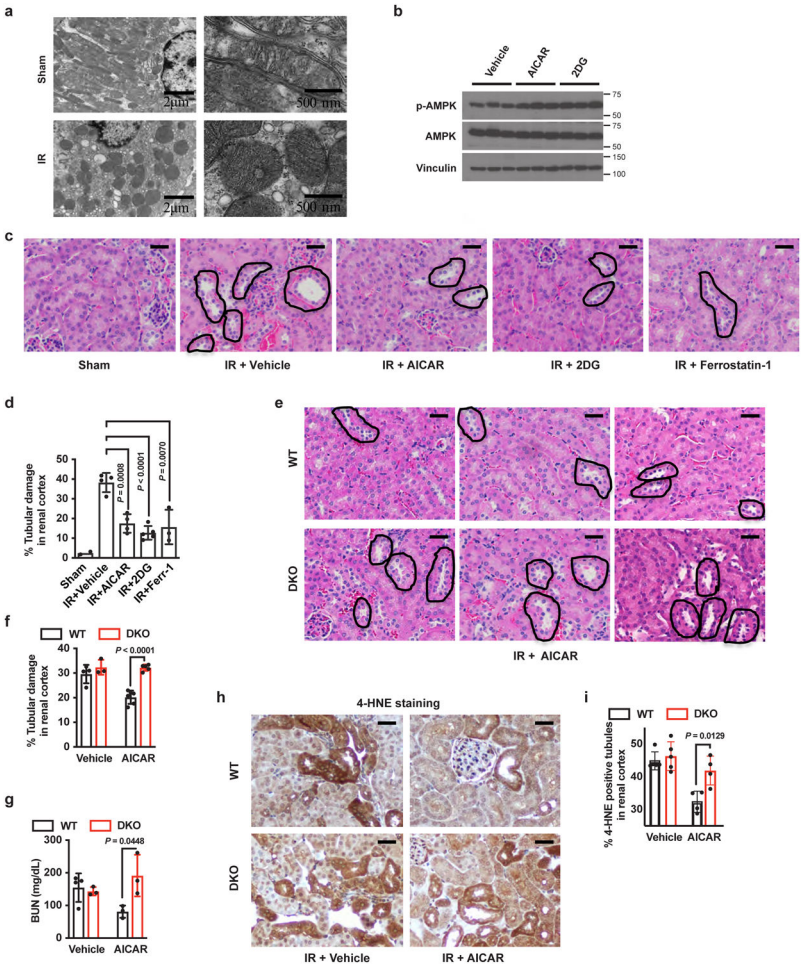

Fig.6. AMPK activation protects renal ischemia reperfusion injury.

a, Transmission electron microscopy of cortical renal tissues from the mice after ischemia reperfusion (IR) or sham-treatment. Scale bars: left, 2 μm; right, 500 nm. The experiment was repeated three times, independently, with similar results. **b-d**, Wild-type mice injected with vehicle, AICAR (0.5 mg/g), 2DG (0.5 mg/g), or Ferrostatin-1 (2 μg/g) were subjected to 30 min IR. Western blot analysis showing AMPK activation in the tissue lysates from mouse kidneys (**b**). The experiment was repeated three times, independently, with similar results (**b**). Representative images of hematoxylin and eosin (H&E) staining of the renal cortex after IR. Black dotted lines, damaged renal proximal tubules (as characterized by tubular dilatation, tubule brush border loss, flattened epithelial cells, or sloughing of cells) (**c**). Scale bars, 50 μm. Bar graphs show percent of tubular damages in the renal cortex (**d**). n = 2 (Sham), n = 3 (IR+Ferr-1), n = 4 (IR+V, IR+AI) or n = 5 (IR+2DG) mice. **e-i**, *AMPK*α1/α2$^{L/L}$ or *AMPKα1/α2*$^{L/L}$, *Rosa26-CreERT2* mice injected with either vehicle or AICAR for 7 days (referred to as *AMPK* WT and DKO mice) were subjected to IR. Representative images of H&E staining showing the damaged renal cortex after IR (**e**). Scale bars, 50 μm. Bar graphs show the percentages of tubular damages (**f**). Data show the mean ± s.d., n = 3 (DKO+vehicle), n = 4 (WT+vehicle), n = 5 (DKO+AICAR) or n = 6 (WT +AICAR) mice. Bar graphs show blood urea nitrogen (BUN) levels (**g**). Data show the mean

± s.d., n = 3 (DKO+vehicle, WT+AICAR, DKO+AICAR) or n = 4 (WT+vehicle) mice. Representative images showing 4-HNE immunohistochemical staining from mouse renal cortex with the indicated genotypes and treatment conditions (**h**; dark brown stained tubules indicate 4-HNE positive staining, Scale bars, 50 μm). Bar graphs showing the percentages of 4-HNE positive tubules per visual field (**i**). Data show the mean ± s.d., n = 4 (AICAR) or 5 (vehicle). Statistical analysis was performed using unpaired, two-tailed t-test. Numerical source data are provided in Source Data Fig. 6. Scanned images of unprocessed blots are shown in Source Data Fig. 6.